TITLE:

Structural analysis of cholesterol binding and sterol selectivity by ABCG5/G8.

AUTHOR NAMES:

Danny Farhat[1,‡], Fatemeh Rezaei[1,‡], Milica Ristovski[1,2,‡!], Yidai Yang[1], Albert Stancescu[1,3,#], Lucia Dzimkova[1,4], Sabrina Samnani[1,4], Jean-François Couture[1] and Jyh-Yeuan Lee[1,*]

AUTHOR ADDRESSES:

[1] Department of Biochemistry, Microbiology and Immunology, Faculty of Medicine, University of Ottawa, Ottawa, Ontario, Canada

[2] Translational and Molecular Medicine Program, Faculty of Medicine, University of Ottawa, Ontario, Ottawa, Canada

[3] Biochemistry Program, Faculty of Health Sciences, McMaster University, Hamilton, Ontario, Canada

[4] Biochemistry Program, Faculty of Science, University of Ottawa, Ottawa, Ontario, Canada

AUTHOR INFORMATION

* Correspondence should be addressed to Jyh-Yeuan (Eric) Lee (Jyh-Yeuan.Lee@uOttawa.ca).

‡ Contributed equally.

Current address: MBiotech Program, University of Toronto-Mississauga

! Current address: Undergraduate Medical Education, Faculty of Medicine, University of Ottawa

ABSTRACT:

The ATP-binding cassette (ABC) sterol transporters are responsible for maintaining cholesterol homeostasis in mammals by participating in reverse cholesterol transport (RCT) or transintestinal cholesterol efflux (TICE). The heterodimeric ABCG5/G8 carries out selective sterol excretion, preventing the abnormal accumulation of plant sterols in human bodies, while homodimeric ABCG1 contributes to the biogenesis and metabolism of high-density lipoproteins. A sterol-binding site on ABCG5/G8 was proposed at the interface of the transmembrane domain and the core of lipid bilayers. In this study, we have determined the crystal structure of ABCG5/G8 in a cholesterol-bound state. The structure combined with amino acid sequence analysis shows that in the proximity of the sterol-binding site, a highly conserved phenylalanine array supports functional implications for ABCG cholesterol/sterol transporters. Lastly, *in silico* docking analysis of cholesterol and stigmasterol (a plant sterol) suggests sterol-binding selectivity on ABCG5/G8, but not ABCG1. Together, our results provide a structural basis for cholesterol binding on ABCG5/G8 and the sterol selectivity by ABCG transporters.

KEYWORDS:

ABCG5, ABCG8, ABCG1, ABCG sterol transporters, cholesterol, sterol selectivity, X-ray crystallography, molecular docking

ABREVIATIONS:

ABC, Adenosine-triphosphate-binding cassette; NBD, Nucleotide binding domain; TMD, Transmembrane domain; TMH, Transmembrane helix; RCT, Reverse cholesterol transport; PH, Phenylalanine Highway

42 **1. INTRODUCTION**

43 Lipid homeostasis in mammalian cells is a critical process regulated in part by the ATP
44 binding cassette (ABC) lipid transporters, particularly the ABCG and ABCA cholesterol
45 transporters, such as ABCG1, ABCG4, ABCG5/G8 and ABCA1. As a critical component of
46 cellular membranes, cholesterol comprises >50% of total cellular lipid content and is further
47 utilized as the precursor molecule for steroid hormones that modulate gene regulation as well as
48 bile acids that are required for nutrient absorption. To maintain cholesterol balance, excess
49 cholesterol must be eliminated from cells and tissues via the reverse cholesterol transport (RCT)
50 pathway by circulating high-density lipoproteins [1–3]. Within the human ABCG protein
51 subfamily, all members function as lipid floppases, with the notable exception of ABCG2, that
52 opts for a more relaxed approach to substrate efflux by working as the sole multidrug transporter
53 (MDR) of the subfamily [4,5]. In addition, the PDR subfamily of full-length transporters (ABCG2
54 homologues in *Saccharomyces cerevisiae*) are related to ABCG and sharing the structural fold and
55 inverted topology. Moreover, ABCG transporters are becoming increasingly important with new
56 findings uncovering their physiological roles in severe chronic diseases, notably such as cancer,
57 atherosclerosis, diabetes and Alzheimer's disease [6–11]. While these proteins have gained more
58 notoriety, the efflux mechanisms have remained a mystery, with various proposed hypotheses that
59 are yet to be agreed upon.

60 In mammals, ABCG lipid transporters consist of the heterodimeric ABCG5/G8 and the
61 homodimeric ABCG1 or ABCG4 complexes. ABCG5/G8 is localized on the canalicular
62 membranes of the bile ducts in the liver and the brush border of enterocytes in the small intestines,
63 where it mediates the final step of the RCT [9,12–14]. ABCG1 and ABCG4 translocate cholesterol
64 within the plasma membrane and in endosomes [15,16] and play a key role in the regulating

65 cholesterol balance in the lung, the brain and in macrophage-rich tissues [17–20]. ABCG5/G8
66 undergoes obligatory heterodimerization and is unique in its capability of preferential efflux for
67 dietary plant sterols over cholesterol [8,9,21,22]. The mechanisms that govern such substrate
68 selectivity within this protein subfamily, however, remains elusive. Based on the crystal structure
69 of ABCG5/G8, we can now theorize that such substrate specificity among ABCG transporters may
70 be the result of the difference in hydrophobic valve composition between the multidrug transporter:
71 ABCG2 and the lipid transporters: ABCG1, ABCG4, ABCG5/G8 [23,24]. In addition, a sterol-
72 binding site was postulated at the membrane-transporter interface based on the crystal structure of
73 ABCG5/G8 [25], whereas studies in recent ABCG1 structures [26,27] have suggested sterol
74 binding at the cytoplasmic end of the transmembrane domain (TMD).

75 The general TMD topology is shared among ABCG subfamily proteins. Each half
76 transporter consists of six transmembrane helices (TMH) and the re-entry helices that are part of
77 the extracellular domains. A connecting helix bridges the TMD to the nucleotide-binding domain
78 (NBD), forming an amphipathic interface on the cytoplasmic leaflet of the lipid bilayers.
79 Meanwhile a triple-helical bundle brings the TMDs and the NBDs together to create a compact
80 and short-stacked transporter conformation [23–25]. At the cellular level, ABC lipid transporters
81 have been shown to alter the composition of their local membrane environment. Such revisions
82 may come from the subduing of lipid rafts by redistributing the high cholesterol content towards
83 the surrounding membrane regions [16,28]. Using *in vivo* and *in vitro* functional assays, we have
84 previously characterized a loss-of-function (LOF) mutation $ABCG5_{A540F}$, a conserved residue near
85 a putative sterol-binding site in ABCG5/G8 [25,29]. These findings suggested the likelihood of an
86 access site that allows the binding of cholesterol binding prior to its re-localization within the
87 membrane-embedded portion of the sterol transporters.

88 One of the significant challenges in studying the cholesterol-transporter interaction is to
89 accurately identify the sterol molecules as either the transport substrates or the intrinsic component
90 of cell membranes. The latter can also play regulatory roles in membrane protein functions, such
91 as ABCG2 [30] or G-protein coupled receptors [31]. Besides experimental approaches to obtain
92 atomic models by crystallography or electron microscopy, *in silico* molecular docking can allow
93 researchers to predict the ligand-binding sites on a protein by using available structural models
94 and ligand libraries. The availability of either ABCG5/G8 or ABCG1 structural can now make it
95 possible to provide a molecular framework and to allow further structural analyses by using *in*
96 *silico* tools, such as molecular docking or molecular dynamics simulation.

97 In this study, we first carried out amino acid sequence analysis of ABCG transporters,
98 highlighting key conserved aromatic residues arranged in a spatially conserved pattern on TMH2.
99 We solved the crystal structure of ABCG5/G8 in complex with cholesterol. The structure shows
100 that an orthogonal cholesterol molecule fitting horizontally in front of A540, a conserved ABCG5
101 residue at this orthogonal sterol-binding site. *In vitro* cholesterol-binding assay showed an
102 inhibition of sterol binding activity by the mutant $ABCG5_{A540F}$/G8. To determine the differential
103 sterol binding activities on ABCG sterol transporters, blind molecular docking analysis was
104 conducted on wild-type (WT) ABCG5/G8 or ABCG1 in the presence of cholesterol or
105 stigmasterol, as well as selective mutants $ABCG5_{Y432F}$, $ABCG8_{N564P}$ and $ABCG5_{A540F}$. We also
106 analyzed the cholesterol-binding patterns on the ATP bound states by using both experimental and
107 homology models, showing the sterols only accumulated on the surface of the extracellular
108 domain, possibly an intermediate state during the ATP-coupled sterol-transport cycle. Together
109 with previous *in vivo* and *in vitro* observations, our results provide a structural basis for sterol
110 selectivity of ABCG lipid transporters and a visual component to the sterol-transport mechanism.

2. RESULTS

2.1 Conserved phenylalanine cluster on THM2 of ABCG transporters:

Recent structural determination of ABCG transporters by cryo-electron microscopy [26,27,32,33] confirms the general molecular architecture as initially revealed by the crystal structure of an apo ABCG5/G8 (Lee et al., 2016). The TMH2 and TMH5 of both subunits are adjacent to one another, forming a dimer interface within the transmembrane domains. This interface has been hypothesized to be a sterol translocation pathway based on sterol localization as observed in the EM structures. However, to what extent this pathway contributes to sterol translocation remains unclear. In this study, we used multiple sequence alignment to analyze the amino acid sequence conservation in the TMH2 of human ABCG1/2/4/5/8, PDR5 of the yeast *Saccharomyces cerevisiae* [34], and White protein of *Drosophila melanogaster* [35,36](**Fig. 1**). Among these seven ABCG transporters, White is a close homologue to ABCG1, while the drug resistant PDR5 is an ABC drug transporter and an ABCG2 homologue. Using ABCG1 as sequence reference and analyzing 300 mammalian orthologs, each ABCG member includes a highly conserved phenylalanine (or tyrosine in ABCG5) at position F1 (**Fig 1A**). The adjacent position F2 shows similar conservation of hydrophobic residues, albeit with a more relaxed sequence homology than F1 (**Fig 1A**). Position F3 reveals a conserved phenylalanine in ABCG1, ABCG4 and the N-terminal half of PDR5 (PDR5-1), although the C-terminal half of PDR5 (PDR5-2) has a conserved phenylalanine just one residue off from F3. Position F4 shows the last highly conserved phenylalanine found on TMH2 (**Fig 1A**). These conserved phenylalanine residues are visualized through a Logo plot (**Fig 1B**), indicating at least two phenylalanine residues being flanked between positions F1 and F4 on the hydrophobic residue-rich TMH2.

When inspecting the spatial relationship of these phenylalanine residues, we observed an

134 open space immediately below the hydrophobic valve and above a cavity that is open to the
135 cytoplasm in the inward-facing conformation of ABCG transporters (**Fig. 1C, left**). Not only are
136 the F1-4 residues shared among the eight homologous monomers, but two or three aromatic side
137 chains also point inwards the TMD dimer interface, creating a highway-shaped open space (**Fig**
138 **1C, right**). We have coined this open space as the Phenylalanine Highway (PH) to highlight this
139 unique structural motif in the transmembrane domain. ABCG1 and ABCG4 share the most closely
140 spaced phenylalanine residues in their iteration of the PH, while the F2 in White is one residue off
141 from that in ABCG1. ABCG2, ABCG8 and PDR5 (either the N- or C-terminal half) have similar
142 spacing of their phenylalanine residues, whereas the equivalent residues on ABCG5 are replaced
143 by aromatic tyrosine residues. In addition, the phenylalanine side chains may be adjusted based on
144 the ligand placements (**Suppl Fig. 1**). Moreover, position F1 is spatially adjacent to the aromatic
145 residues of the previously described hydrophobic valve (or ABCG2's di-leucine valve/gate),
146 forming a closed interface in the inward-facing protein conformation (**Fig 1D & 1E**) [23]. It may
147 be possible to speculate that with such close spatial proximity, interaction between the
148 hydrophobic valve and the phenylalanine residues could occur during the catalytic cycle via certain
149 conformational changes. Further investigation is needed to address this question.
150
151 *2.2 Crystal structure of ABCG5/G8 in an orthogonal cholesterol-binding state:*
152 Several *bona fide* sterol molecules were observed on recent cryo-EM structures of ABCG1
153 or ABCG5/G8, which led to various models of their sterol-transport (or binding) mechanisms, but
154 more structural data and further mechanistic analysis are still required to establish a convergent
155 model of cholesterol transport. We have previously crystallized human ABCG5/G8 in an apo state
156 by bicelle crystallization. To gain the structural basis of the sterol-transport (or binding)

157 mechanism, in this study, we determined a cytoplasmic-facing crystal structure of cholesterol-
158 bound ABCG5/G8 at 4Å by X-ray crystallography. Three X-ray diffraction datasets were
159 integrated and scaled with acceptable statistics. The initial model was obtained by molecular
160 replacement using a previously resolved cryo-EM structure (PDB ID: 7JR7) [33], and the motifs
161 involved in ATP binding were adjusted based on the previous crystal structure (PDB ID: 5DO7)
162 [25]. Two ABCG5/G8 heterodimers are observed in the asymmetric unit. The protein model in
163 this report includes a corrected amino acid registry in the nucleotide-binding domain as previously
164 highlighted by Zhang *et al.* Additionally, it shows a consistent overall architecture and key
165 structural features as described previously, overall root mean square deviation (RMSD) of ~0.9 Å
166 when superimposed [12,25,33](**Suppl. Fig. 1A**). After initial refinement, we observed two clear
167 electron densities at the interface of symmetrically located transmembrane domains of these two
168 transporters, which resembled the polycyclic characteristic of cholesterol molecules. Therefore,
169 we added two cholesterol molecules to the initial model for further refinement and obtained a
170 significant improvement of the Rfree from 0.338 to 0.302 and reasonable geometrical validation
171 at current resolution. The final model shows an orthogonal cholesterol molecule in close contact
172 with $ABCG5_{A540}$ (namely the ABCG5-dominant side), with the 3-β-hydroxyl group forming a
173 weak hydrogen bonding with the side chain of $ABCG8_{T430}$ (4.3-4.5 Å). No sterol was observed on
174 the equivalent side of ABCG8 (namely the ABCG8-dominant side) (**Fig. 2A**). Selected regions of
175 the electron densities are shown in Suppl Fig. 2. The statistics of data processing and model
176 refinement are summarized in **Table 1**.
177
178 With an *in vivo* analysis of biliary cholesterol secretion and an *in vitro* ATPase assay, we
179 have previously characterized a loss-of-function (LOF) mutant $ABCG5_{A540F}$/G8 (A540F),
180 predicting a putative sterol-binding at this transporter-membrane interface [25,29]. In this study,

181 we developed an *in vitro* cholesterol-binding assay using tritiated cholesterol (see Materials and
182 Methods) and characterized cholesterol binding on purified ABCG5/G8 WT and A540F mutant
183 proteins (**Fig. 2B**). The reaction reached a saturation of cholesterol at ~3 μM with the B_{MAX} as
184 50.64±0.77 CPM, where the mutant showed about two-fold inhibition of the maximal cholesterol-
185 binding rate. The binding constant K_D and Hill coefficient h were estimated as 1.46 ± 0.28 μM (h
186 = 2.91) and 1.55 ± 0.01 μM (h = 2.98) for the WT and mutant proteins, respectively. Given the
187 ATPase activity of A540F mutation was suppressed by ~90% with similar K_M for sterols [29],
188 both assays suggest a functionally defective conformation by this LOF mutant. Together with the
189 new structural data, our analysis supports the role of the orthogonal cholesterol-binding site in
190 proximity to $ABCG5_{A540}$ (**Fig. 2**).
191
192 *2.3 Asymmetric binding of cholesterol or stigmasterol on ABCG5/G8, but not ABCG1:*
193 The ABC transporter superfamily translocate a broad spectrum of substrates across cellular
194 membranes, with individual members conveying their unique substrate specificities. To determine
195 how ABCG transporters bind sterol ligands, we used previously published apo models ABCG5/G8
196 (PDB ID: 5DO7 or 7JR7) and ABCG1 (PDB ID: 7R8D) [25,33] and carried out molecular docking
197 on the TMD with cholesterol or stigmasterol, a plant sterol previously shown to have the highest
198 accumulation rate in an Abcg5/g8-deficient mouse model [37]. Using UCSF DOCK6 suite [38],
199 we first optimized the docking protocol by carrying out a redocking of the ligands (topotecan,
200 mitoxantrone and imatinib) to reproduce their complex with ABCG2. Additional redocking was
201 done on a distinct ABCG2 model to further evaluate docking optimization. (**Suppl Fig. 3**) [39,40].
202 Figure 3 shows the docking results of all acceptable (or viable) poses for the two sterol
203 ligands, cholesterol and stigmasterol, on the ABCG sterol transporters according to the standard

204 flexible docking protocol as implemented in DOCK6 suites [38]. On ABCG5/G8, poses of sterols
205 are distributed asymmetrically at the opposing membrane-transporter interfaces, having more
206 docking conformations on the ABCG5-dominant side (**Fig. 3A/B**). The predicted orthogonal
207 cholesterol (*i.e.*, one of the top-3 poses) has a nearly identical position to the cholesterol molecule
208 in the newly determined cholesterol-bound structure (**Fig. 2 & 3D/E**). On the ABCG8-dominant
209 side, no orthogonal sterol was obtained, and either ligand are clustered on the inner leaflet of the
210 membrane's lipid-bilayered and with the topmost sterols in close distance from the lower end of
211 the PH (*i.e.*, $ABCG5_{Y432}$ or $ABCG1_{F455}$). Such asymmetric sterol binding on ABCG5/G8 suggests
212 another level of functional asymmetry by ABCG5/G8-mediated sterol transport. On the ABCG1
213 homodimer, acceptable poses are only observed on the inner leaflet of the lipid-bilayered
214 membranes, resembling those on the ABCG8-dominant side, and bound sterols can be equally
215 distributed on either side of the transporter-membrane interface (**Fig. 3A/B, bottom**). Such
216 symmetric sterol binding is distinct from ABCG5/G8, suggesting different mechanisms of using
217 the PH between ABCG1 and ABCG5/G8.

218 To analyze sterol docking with ATP-bound structures, we performed the analysis on an
219 ATP-bound ABCG1 and a homology model of ATP-bound ABCG5/G8 (see Materials and
220 Methods) [41]. Surprisingly, given the same docking grid as used for apo structures, sterol docking
221 on the ATP-bound ABCG1 or ABCG5/G8 only showed clusters on top of the extracellular
222 domains of the extracellular-facing structures and far away from the PH (**Fig. 4A/B**). As current
223 apo or ATP-bound structures of ABCG sterol transporters are rather limited to early and end states
224 of catalysis [25–27,33], the sterol poses as observed here may represent the post-efflux
225 conformations where the previously observed ligand binding sites have become inaccessible due
226 to the compression of protein's interfacial cavity in these ATP-bound structures. For this reason,

227 binding sites within the protein were unable to be detected and subsequently docked. We
228 additionally utilized MOLE2.5 [42] to determine the volume of cavities detected within the TMD.
229 In ABCG1 cavities substantially large were found in between the transmembrane helices, however
230 these were away from the central canal of the protein (**Suppl Fig. 5B**, left). In ABCG5/G8, while
231 one big cavity appeared within the central canal of the protein, it was found to be a conglomeration
232 of multiple spheroidal shaped cavities bridged together by very thin regions. Each cavity on its
233 own was presented to be far too small of a volume at around ~200Å^3 comparing to the volume of
234 cholesterol (**Suppl Fig. 5B**, Right), being ~627Å^3 [43]. Our data thus emphasizes the need for
235 occluded turnover state models, as seen in ABCG2 models [44].
236
237 *2.4 Sterol selectivity by ABCG1 and ABCG5/G8:*
238 Among mammalian ABCG sterol transporters, ABCG5/G8 is known to promote
239 absorption of cholesterol but not dietary sterols in the gastrointestinal tract [9]. To study such sterol
240 selectivity, we analyzed the distributions of the sterol-binding poses from the docking experiments
241 by using ABCG1 and ABCG5/G8 as model systems. On ABCG1, cholesterol cluster was gathered
242 uninterruptedly around F455, *i.e.*, F4 of PH, and docked similarly on both sides of the transporter-
243 membrane interface. The sterol cloud is angled towards the putative sterol binding cavity at the
244 NBD-TMD interface, in the membranes lower leaflet. (**Fig. 3A, bottom**). Stigmasterol equally
245 shows the same angling into the binding site, but with reduced possible poses when compared to
246 cholesterol on ABCG1 (**Fig. 3B, bottom**). The largest number of positions for cholesterol or
247 stigmasterol are located immediately below the PH and above the NBD-TMD interface, suggesting
248 a common sterol-binding cavity in ABCG sterol transporters. However, the orientation the
249 hydroxyl group on the sterols is not necessarily exposed to the aqueous milieu (**Fig. 3A/B,**

250 **bottom**).

251 On the ABCG5-dominant side of ABCG5/G8, stigmasterol binds in two clusters
252 partitioned between each monomer, leaving a gap in the middle, which is opposite to the
253 continuous cloud as revealed by cholesterol (**Fig. 3A/B, top**). In general, there are more possible
254 binding poses in the vicinity of $ABCG5_{A540}$ and ABCG8's PH, where interestingly all sterol
255 molecules appear to orient in a similar direction, *i.e.*, the hydroxyl group pointing to the NBD-
256 TMD interface. On the other hand, on the ABCG8-dominant side and near F4 of ABCG5's PH,
257 the sterol molecules are oriented in various but seemingly unspecific directions (or conformations)
258 (**Fig. 3A/B**). When compared to cholesterol which binds in two separate pockets (**Fig. 3A, top**),
259 stigmasterol has three binding pockets across both sides of the transporter-membrane interfaces
260 (**Fig. 3B, top**). Interestingly, the highest clusters of stigmasterol and cholesterol are located on the
261 opposite sides of the transporter, suggesting preferred association of sterol species on either side
262 of the transporter-membrane interface.

263 $ABCG1_{F455}$ and $ABCG5_{Y432}$ are at the equivalent position F4 of the PH. When comparing
264 the sterol binding patterns around these key residues, more cholesterol poses can be found around
265 $ABCG1_{F455}$ in an increasingly linear shape, while more stigmasterol poses were observed around
266 $ABCG5_{Y432}$ in a "C" shape (**Fig. 3A/B**). In the nucleotide-free structures as used for analysis here,
267 sterol binding in general is positioned more towards the orthogonal sterol-binding site in
268 ABCG5/G8 than in ABCG1. Sterol poses in ABCG1 cluster closer to the central cavity, around
269 PH's F4, while sterols bind ABCG5/G8 closer to the transporter-membrane interface (**Fig 3C**).
270 The sterols of the top binding poses all have hydroxyl groups pointing outwards and away from
271 PH's F4 position. Interestingly, the cholesterol molecules are similarly angled in both ABCG1 and
272 ABCG5/G8, *i.e.,* in parallel to the lipid bilayers.

273 *2.5 Alteration of ABCG5/G8 cholesterol-binding activity by the LOF mutant A540F:*

274 By exploiting the LOF mutant A540F, *in vivo* and *in vitro* functional studies support the
275 notion that it is exposed to the orthogonal cholesterol-binding site [25,29] (**Fig. 2**). Using
276 molecular docking and homology modelling, it is possible to develop hypotheses for the structural
277 basis of how this mutation impacts ABCG5/G8 function. In this study, we analyzed the effects of
278 inducing the A540F mutation on the binding positions of cholesterol as compared to in WT
279 ABCG5/G8 (**Fig. 5**). In the WT protein, the cholesterol cloud stretches from proline 415 (P415,
280 end of the connecting helix of ABCG8 and a landmark position) to A540 (**Fig. 5A**), with one of
281 the top poses being the orthogonal sterol adjacent to A540. The remaining top-three are vertically
282 oriented, exposing the hydroxyl group to the orthogonal sterol-binding site (**Fig. 5B, right & Fig.
283 5C**). Using a homology model containing the A540F mutation, the second and third best binding
284 positions were missing, leaving a gap between PH's F4 and the orthogonal sterol-binding site (**Fig.
285 5B, left & 5C**). As mutation was induced, the orientation of the orthogonal cholesterol is flipped
286 180° at the sterol-binding site (**Fig. 5D/E**), and the remaining non-top three poses have their
287 hydroxyl groups pointing to the cytoplasmic side of the lipid bilayer (**Fig. 5B**). Overall, lower
288 number of different cholesterol poses were docked on the mutant as compared to the WT protein.
289 The microenvironment surrounding the orthogonal cholesterol on A540F mutant are highlighted
290 in **Figure 5E**, showing that the phenylalanine substitution prevents the interactions between the
291 cholesterol and polar residues (*e.g.*, $ABCG8_{T430}$) that may attract the hydroxyl group in the WT
292 protein.

293

294 *2.6 Lower transmembrane sterol-binding cavity in ABCG5/G8:*

295 The recent cryo-EM structural determination of ABCG1 suggested a cholesterol-binding

296 cavity in the cytoplasmic leaflet of the bilayer [26,27]. The protein's surface within the binding
297 cavity in ABCG1 shows a narrow gap that is wider than corresponding cavity found in ABCG5/G8
298 (**Fig. 6A**); additionally, this cavity is located immediately below F4 of the PH (**Fig. 6B**). In the
299 WT proteins, $ABCG5_{Y432}$ and $ABCG8_{N564}$ are separated by 4.0 Å, whereas the equivalent positions
300 in $ABCG1_{F455}$ and $ABCG1_{P558}$ are farther separated by 6.9Å. We created an ABCG5/G8 homology
301 model that consists of mutations $ABCG5_{Y432F}$ and $ABCG8_{N564P}$ to mimic an ABCG1-like cavity.
302 The interaction between the mutant residues in ABCG5/G8 are at a similar distance and positions
303 to the corresponding residues in ABCG1 (**Fig. 6B/C**). This distance is significantly widened from
304 4.0 Å to 6.9 Å in the mutant. Due to the increased distance between the residues, the double mutant
305 lacks the ability to form such N-Y blockade and results in a deeper cavity than that of WT. We
306 then performed sterol docking analysis on this double-mutant model and analyzed the possible
307 sterol conformations in this cytoplasmic sterol-binding cavity. In the WT, stigmasterol appears to
308 bind more readily than cholesterol, where the cluster of docked stigmasterol poses is much bigger
309 than the cholesterol cloud (**Fig. 6D/E**). Both sterol clouds semi-encircle Y432 in a "C" shape.
310 When Y432 is mutated to phenylalanine, the number of docked sterols decreased significantly as
311 compared to the WT, simply localizing overhead of position 432 and suggesting lower sterol-
312 binding ability in the mutant. Interestingly, the size of viable poses becomes more alike for either
313 cholesterol or stigmasterol. Despite using $ABCG5_{Y432F}/G8_{N564P}$ mutations to mimic the width of
314 the cavity found in WT ABCG1, the binding pattern in the mutant does not resemble that of
315 ABCG1 (**Fig. 2A and Fig. 2B, bottom**), suggesting the possibility of either sterol transporter
316 adopting multiple conformations to bind sterols throughout the transport cycle. Further functional
317 assays are necessary to define the role of these residues and how they can obstruct sterol
318 translocation trough the cavity.

319

320 **3. DISCUSSION**

321 Atomic models of ABCG sterol transporters have provided the molecular framework to
322 study how individual transporter proteins translocate different substrates. Yet, the location and
323 methods by which these transporters bind sterols remains elusive and controversial. This is
324 particularly true in the case of ABCG5/G8, which is believed to identify and bind plant sterols
325 differently from cholesterol. Understanding how sterols binds on ABCG5/G8 and its homologs
326 will allow us to study the impact of such sterol selectivity on the regulation of sterol transport. In
327 this study, we have determined a cholesterol-bound crystal structure of ABCG5/G8, showing an
328 orthogonal cholesterol binding on the ABCG5-dominant side at the transporter-membrane
329 interface (**Fig. 2**). A mutant $ABCG5_{A540F}$ was previously demonstrated to downregulate biliary
330 cholesterol efflux *in vivo* [25] and to inhibit sterol-coupled ATPase activity *in vitro* [29]. The
331 crystal structure herein provides a structural evidence of this peripheral sterol binding site where
332 a sterol molecule makes direct contact with the conserved $ABCG5_{A540}$ residue (**Fig. 2 & 5**). The
333 sterol fits into an indented planar cleft within the upper region of the vestibule formed by the re-
334 entry and the transmembrane helices. The captured cholesterol extends across the interfacial space,
335 with its hydroxyl group forming a hydrogen bond with $ABCG8_{T430}$, while the hydrocarbon tail
336 remains straight and in contact with hydrophobic residues on ABCG5, such as L516, L537, I562,
337 F565 and F567 (**Fig. 5D**). We also showed an inhibition of the cholesterol-binding activity by the
338 A540F mutant (**Fig. 2C**). The K_D value is similar for both WT and mutant proteins, echoing the
339 similar K_M for sterol-coupled ATPase activity in previous studies, given the mutant suppressed
340 ATP hydrolysis by ~90% [29]. Taken together with a 180° flipping of cholesterol by this mutant
341 (**Fig. 5E**), current structural and functional data suggest a functionally defective conformation by

342 this LOF mutant, inhibiting both sterol and ATP associations to the transporter. The Hill
343 coefficient was estimated as ~3, although no evidence so far shows whether the transporter bind
344 one or multiple sterol molecules. Further structural and functional studies will be necessary to
345 determine how these sterols bind ABCG5/G8.

346 In a separate experiment, cholesterol was docked to the TMD of previously published
347 ABCG5/G8 structures (PDB ID: 5DO7 or 7JR7) [25,33], where one of the top-3 predicted poses
348 binds to the transporter in similar conformation as revealed by the crystal structure (**Fig. 3D/E**).
349 The core steroid rings and the hydroxyl group matched in similar tilt, although the hydrocarbon
350 tail varied slightly with minimal rotation. The latter may be explained by its relatively high
351 mobility, such that the deviation was expected. Using a homology model containing the A540F
352 mutation, the large aromatic group in position 540 introduced steric hindrance, consequently
353 disabling cholesterol docking onto the observed position as shown in the crystal structure or
354 predicted docking on WT protein (**Fig. 2 & 3**). In addition, cholesterol docking with the A540F
355 mutant resulted in a loss of top-3 poses as seen on the WT protein. Altogether, past and present
356 data support the existence of an orthogonal cholesterol binding site located around residue
357 $ABCG5_{A540}$, and the orthogonal sterol poses may be part of intermediate states of sterol-
358 translocation trajectory along the TMD.

359 Via a protein sequence analysis of primarily mammalian ABCG transporters, we have
360 identified a structural motif, "phenylalanine highway" along the TMH2 that consists of conserved
361 aromatic residues (usually phenylalanine) (**Fig. 1**). This motif is flanked by two highly conserved
362 aromatic residues (*i.e.*, positions F1 and F4), where position F4 appears to involve in sterol
363 capturing from the cytoplasmic end of the membranes (**Suppl Fig. 1)** and the PH may provide a
364 pathway for docked sterols to enter the dimer's interface (**Fig. 3**). Although not fully defined,

365 certain PH residues are believed to form a molecular clamp previously shown to mediate π–π
366 interactions with sterol molecules [39,41,45,46]. As substrates for ABCG tend to be polycyclic
367 with more or less an aromatic group that can interact with aromatic amino acids, the PH motif
368 possibly serves as a conserved molecular clamp of ABCG sterol transporters (**Fig. 1C**). The clamp-
369 like role of the lower PH terminus was recently suggested by structural studies of ABCG1 and
370 ABCG2. The ATPase activity of ABCG1 was inhibited by $ABCG1_{F455A}$ mutation [27], while
371 ABCG2-driven drug efflux was downregulated by $ABCG2_{F439A}$ mutation [46]. Interestingly,
372 mutation $ABCG2_{F439Y}$ or $ABCG2_{F439W}$ did not hamper the efflux function, emphasizing the
373 importance of aromatic residues in contributing to a substrate-binding route from the inner leaflet
374 of the membranes [46]. In ABCG5/G8, while the clamp-like function of $ABCG5_{Y432}$ has yet to be
375 showcased, our docking analysis and a previous *in vivo* data suggest its biochemical nature as a
376 key feature for the transporter function, presumably sterol binding. In this study, a double-mutant
377 model ($ABCG5_{Y432F}$/$ABCG8_{N564P}$) revealed a loss of the ability to form a hydrogen bonding at the
378 TMD dimer interface of the protein model (**Fig. 6B**) and a deeper cavity was formed to imitate
379 ABCG1, yet the overall binding patterns were adversely affected (**Fig. 6D/E**). While the
380 physiological impact of this double mutation has yet to be determined, such pair nonetheless
381 created a blockade in the cavity of ABCG5/G8's model. Since docking utilizes static protein
382 models, widening of the cavity through mutation helped to mimic the effects of possible dynamic
383 protein movement causing the subsequent fracture of the physical hindrance. This alteration in
384 binding conformations and obstruction of the molecular clamp may help explain why *in vivo*,
385 $ABCG5_{Y432A}$/$ABCG8_{WT}$ caused a significant decrease in biliary cholesterol efflux [25]. The
386 mutations we had modelled retained the aromatic group; the *in vivo* data thus suggested a loss of
387 the molecular clamp at the lower PH terminus. It is important to note that $ABCG5_{Y432}$ is also part

388 of the TMD polar relay network [23,29]. Unlike the ABCG8 equivalent ($ABCG8_{F461}$), $ABCG5_{Y432}$
389 may play a dual role in the sterol binding/translocation and the allosteric regulation that couples
390 ATPase and sterol-transport activities [29].

391 The upper PH terminus (*i.e.*, $ABCG5_{Y424}$ and $ABCG8_{F453}$) lies immediately under the
392 hydrophobic valve (**Fig. 1D/E**), suggesting a cooperativity between PH's F1 position and the
393 hydrophobic valve in the sterol-transport function. $ABCG5_{Y424}$, $ABCG8_{F453}$ and $ABCG1_{F447}$ all
394 extend their side chains towards the valve's aromatic residues, forming aromatic-aromatic
395 interactions as suggested previously [27]. In ABCG1 and ABCG4, the di-phenylalanine valve may
396 grant the possibility of aromatic interactions between the neighboring six phenylalanine residues.
397 In contrast, the leucine and methionine from ABCG5/G8's hydrophobic valve provide an
398 asymmetric gating of sterol transport, as opposed to the symmetric valve in ABCG1 or ABCG4.
399 In ABCG2, the lack of any phenylalanine within its di-leucine valve denies π–π interactions,
400 although $ABCG2_{F431}$ (PH's F1) was shown to engage in drug-protein interactions with ABCG2
401 inhibitors [40]. Position F2 in the PH is moderately conserved **(Fig. 1A)**, although residues at this
402 position has been proposed to involve sterol interactions, as suggested by decreased cholesterol
403 efflux in the presence of $ABCG1_{F448A}$ mutant [32] or drug interaction in ABCG2 [47].
404 Interestingly, such a PH-like motif may not be limited to ABCG sterol transporters. We have
405 observed similar phenylalanine spacing on the structures of other cholesterol-binding or -transport
406 proteins, including ABCA1, ABCA7, SIDT1, SIDT2, PTCH1, and NPC1 (**Suppl Fig. 4**) [34,48–
407 51]. The PH structural motif may be more common than expected, and further studies will be
408 needed to define its functional roles.

409 The docking experiments in this study have allowed us to analyze different binding profiles
410 of cholesterol or stigmasterol on ABCG1 and ABCG5/G8 (**Fig. 3**). Previous *in vivo* studies showed

411 that stigmasterol efflux by ABCG5/G8 was the fastest among dietary plant sterols [37]; hence
412 stigmasterol was used to analyze phytosterol/plant sterol binding to ABCG transporters. Both
413 proteins share cholesterol as a substrate yet deviate in phytosterol transporting abilities.
414 ABCG5/G8 is a known phytosterol transporter, and each transporter-membrane interface has a
415 distinct selectivity for one of the two docked sterols (**Fig. 3A/B**). In comparison, ABCG1 showed
416 similar binding conformations between stigmasterol and cholesterol, with a decreased amount of
417 stigmasterol binding poses on ABCG1 than ABCG5/G8. Together, our results indicate that sterol
418 selectivity not only occurs on the opposite transporter-membrane interfaces but also differentiate
419 ABCG5/G8 from other ABCG sterol transporters. In addition, our simulation showed the
420 hydrocarbon tail of sterol molecules leading to the PH along with the TMD dimer interface, rather
421 than the hydroxyl group as seen in previous cryo-EM structures of ABCG1 [27]. However, at least
422 one docking pose on the ABCG8-dominant side horizontally points its hydroxyl group to the dimer
423 interface, similar to that of a recent cryo-EM structure **(Suppl Fig. 5A)**. We speculate that the
424 cholesterol orientation as seen in the cryo-EM structures may represent an intermediate
425 cholesterol-binding state among the docked poses (**Fig. 5**).

426 Studies on cholesterol redistribution in lipid rafts have suggested a TMD sterol access site
427 in ABCG1 (**Fig. 4**) [16,28,52]. Theoretically, ABCG1 intakes sterols from enriched lipid
428 microdomains, relocating them towards the surrounding sterol-deprived membranes. The docking
429 pattern follows the amphipathic nature of the lipid bilayers with cholesterol's polar head localizing
430 around the cytoplasmic matrix **(Fig. 3)**, where. cholesterol's hydroxyl group is believed to generate
431 hydrogen bonds with the surrounding polar lipid regions, orienting the sterols head towards the
432 hydrophilic region [53]. Our docking analysis suggests ABCG1's apparent preference for the inner
433 leaflet sterols [16], where the transporters then translocate cholesterol to the upper leaflet, similar

434 to the recently proposed mechanism [26,32]. In ABCG5/G8, both crystallographic and docking
435 results indicated that sterol binding is not limited to the TMD cavity open towards to the
436 cytoplasmic side, but an orthogonal sterol-binding state is a possible intermediate state to drive
437 sterol efflux. As the TMD dimer interface in ABCG5/G8 is much narrower than that in ABCG1,
438 it is possible that ABCG5/G8 similarly uptakes sterol substrates as ABCG1. Still, sterols would
439 need to undergo a series of yet-to-be characterized movements from their longitudinal orientations
440 to an orthogonal binding state as shown in the cholesterol-bound structure (**Fig. 2 &3**). Among
441 ABCG5/G8 substrates, plant sterols may show higher binding preferences as suggested by
442 stigmasterol poses (**Fig. 3**).

443 In conclusion, our crystallographic and computational analysis have highlighted possible
444 regions of sterol binding and interactions on ABCG5/G8. This study shows a conserved
445 phenylalanine highway motif on TMH2 that may play an essential role in substrate recruitment
446 and binding and a crystal structure revealing an orthogonal cholesterol bound on the ABCG5-
447 dominant transporter-membrane interface, consistent with the leading cholesterol poses predicted
448 by molecular docking. The docking analysis of cholesterol and stigmasterol also suggested the
449 asymmetric sterol-binding potential on ABCG5- and ABCG8-dominant transporter-membrane
450 interfaces, and difference in sterol-docking patterns may contribute to different substrate
451 specificity between ABCG1 and ABCG5/G8. Further structural and functional studies will reveal
452 more insight into sterol selectivity and translocation trajectory by ABCG sterol transporters.

453 **4. MATERIALS AND METHODS**

454 *4.1 Protein purification and crystallization*

455 For purification of human WT ABCG5/G8 from *Pichia pastoris* yeast, we have followed
456 the procedures based on our previously reported protocol [25]. With minor modifications, the
457 procedures are briefly described in the following. For each purification, six litres of yeast cell
458 culture were used for ~200 mL of the microsomal membrane preparation at the total protein
459 content of ~10 mg/mL. The membranes were solubilized by equal volume of the solubilization
460 buffer (50 mM Tris-HCl, pH 8.0, 100 mM NaCl, and 10% glycerol, 2% (w/v) β-dodecyl maltoside
461 (β-DDM, Anatrace), 0.5% (w/v) cholate (Sigma-Aldrich), 0.25% (w/v) cholesteryl hemisuccinate
462 Tris (CHS-Tris, Anatrace), 5 mM imidazole, 5 mM β-mercaptoethanol (β-ME), 2 μg/ml leupeptin,
463 2 μg/ml pepstatin A, 2 mM PMSF). Insoluble membranes were removed by ultracentrifugation,
464 and the solubilized supernatant was treated with a final concentration and 0.1 mM Tris (2-
465 carboxylethylcarboxyethyl) phosphine (TCEP). Following that, tandem affinity chromatography
466 was performed. The soluble membrane proteins were separated using a 20-mL nickel-
467 nitrilotriacetic acid (Ni-NTA) column. Then, the peak fractions of ABCG5/G8 from the Ni-NTA
468 eluates were mixed with the equal amount of CBP column wash buffer (50 mM HEPES, pH 7.5,
469 100 mM NaCl, 0.1% (w/v) β-DDM, 0.05% (w/v) cholate, 0.01% (w/v) CHS (Steraloids), 0.1 mM
470 TCEP ,1 mM $CaCl_2$, 1 mM $MgCl_2$) and then loaded onto a 5-mL CBP column. The CBP column
471 was washed sequentially to exchange detergents to DMNG, and ABCG5/G8 proteins were finally
472 collected using an elution buffer (50 mM HEPES, pH 7.5, 300 mM NaCl, 2 mM EGTA, 0.1%
473 (w/v) DMNG, 0.05% (w/v) cholate, 0.01% (w/v) CHS, 1 mM TCEP). The N-linked glycans and
474 the CBP tag were cleaved by endoglycosidase H (Endo H, ~0.2 mg per 10–15 mg purified protein,
475 New England Biolabs) and HRV-3C protease (~2 mg per 10–15 mg purified proteins) for

476 overnight at 4 °C. The CBP tag-free proteins were further purified by gel filtration chromatography
477 using an ÄKTA Purifier and a Superdex 200 30/100 GL column in the buffer containing 10 mM
478 HEPES, pH 7.5, 100 mM NaCl, 0.1% (w/v) DMNG, 0.05% (w/v) cholate, 0.01% (w/v) CHS. The
479 peak fractions were pooled together and treated by reductive methylation. The methylated proteins
480 were relipidated by overnight incubation with 0.5 mg/ml DOPC: DOPE (3:1, w/w) and further
481 purified by a 2-mL Ni-NTA column, followed by iodoacetamide treatment for cysteine alkylation.
482 The relipidated proteins were treated with 1 mM AMPPNP (sodium salt, Roche) for overnight at
483 4 °C and desalted with a PD-10 column. The desalted and lipidated proteins were incubated
484 overnight with cholesterol (prepared in isopropanol) to a final concentration of ~20 μM, and
485 protein precipitants were removed by ultracentrifugation for 10 min at 4 °C. Using 100 kDa cutoff
486 filters, the supernatants were concentrated to a final protein concentration of 30-50 mg/ml and
487 crystallized within a week.

488 Protein crystal growth was carried out by bicelle crystallization as described previously.
489 Briefly, the cholesterol-treated ABCG5/G8 proteins were reconstituted into 10% DMPC/CHAPSO
490 bicelles (lipids and detergents in a 3:1 (w/w) ratio, with the lipids containing 5 mol% cholesterol
491 and 95 mol% DMPC). After that, the proteins and bicelle stock were gently mixed in a 1:4 (v/v)
492 ratio, resulting in a final protein concentration of ~10 mg/ml. At 20 °C, the crystallization was
493 done in a hanging-drop vapor diffusion technique by mixing protein/bicelle preparation with
494 equal-volume crystallization reservoir solution containing 1.8–2.0 M ammonium sulfate, 100 mM
495 MES pH 6.5, 2–5% PEG400, and 1 mM TCEP. Protein crystals were harvested within 1-2 weeks
496 of incubation by first submerging the crystals with 0.2 M sodium malonate and then flash-freezing
497 the crystals in liquid nitrogen with Mitegen cryoloops.

498

499 *4.2 Data collection of X-ray diffraction, structural determination and refinement*

500 X-ray diffraction data were collected using beamlines 19-ID on a Quantum 315r detector
501 at the Advanced Photon Source (APS). Scaling and integration of three datasets were carried out
502 by HKL2000 software package, and the final data was scaled between 30Å and 4Å resolutions to
503 ensure I/σ >1 [54]. Using Phaser program, we obtain the phase information and a structural
504 solution by molecular replacement using a cryo-EM structure (PDB ID: 7JR7) as the initial
505 template [33,55]. Before model refinement by Phenix, the Phaser solution was corrected at the
506 Walker A, the Walker B, and the Signature motifs by the more defined registry in the crystal
507 structure (PDB ID: 5DO7) [25,56]. The initial refinement resulted in a refined model with Rfree
508 and Rwork of 0.338 and 0.309, respectively. Close inspection of the Fo-Fc map, two orthogonal
509 electron densities that clearly include the nature of polycyclic rings were observed between the
510 crystallographic dimer interface and on the ABCG5-dominant side where each electron density is
511 within the van der Waals' distance from $ABCG5_{A540}$. No such electron densities were observed on
512 ABCG8-dominant side. We thus modeled a cholesterol molecule per electron density, and we
513 refined the structure in the presence of one cholesterol molecule on each ABCG5/G8 heterodimer
514 by testing a series of sterol orientations using the program COOT [57]. Following our final
515 refinement, Rfree and Rwork were determined to be 0.302 and 0.244, respectively. The model
516 quality was validated by MolProbity as implemented in Phenix [56,58]. As a note, given the
517 proteins were co-crystallized with AMPPNP, we were not able to observe obvious electron
518 densities for the nucleotides from the current datasets at the current resolution.

519

520 *4.3 Protein sequence analysis*

521 All FASTA files were acquired using PSI-BLAST (position-specific iterated basic local

522 alignment search tool) as implemented in the NCBI protein sequence database. All queries were
523 acquired such that the organism belonged to the Mammalia family, and all partial and incomplete
524 queries were filtered out. FASTA sequences were then surveyed one by one to ensure that the
525 search criteria were executed properly, and no incomplete sequences were passed. FASTA
526 sequences were acquired for ABCG1, ABCG2, ABCG4, ABCG5, and ABCG8 (P45844,
527 Q9UNQ0, Q9H172, Q9H222, Q9H221) with the following PSI-BLAST search query:
528 *"ABCXY"[Gene] AND "Mammalia"[Organism] NOT "partial"[All Fields],* Whereby X denotes
529 the ABC subfamily, and Y denotes the member protein. Including 250-300 species, all alignments
530 and analyses were run locally using the Bio Python repository [59]. A multiple sequence alignment
531 (MSA) was conducted using all the FASTA sequences using a BLOSUM62 substituation matrix
532 [60], ClustalW [61] or PROMALS3D [62]. To score conservation, alignment files were made of
533 the FASTA sequence library using the Multiple Sequence Comparison by Log-Expectation
534 (MUSCLE) tool [63]. To generate a consensus sequence, a "dumb consensus" was conducted with
535 a default threshold of 70% and a required multiple of 1. Consensus sequences were acquired for
536 mammalian ABCG1, ABCG2, ABCG4, ABCG5, and ABCG8. Consensus sequences for each
537 protein subfamily and member were compared to one another to determine highly conserved amino
538 acids and amino acid sequences. For example, the amino acids present in the consensus sequence
539 of ABCG1 was individually aligned to ABCG2, ABCG4, ABCG5, and ABCG8. Conservation
540 scores above the set threshold (80%) were extracted for analytical purposes. An 80% similarity
541 threshold, as opposed to 70%, was used using AMAS method of multiple sequence alignment
542 because this analysis compared two consensus sequences together, 80% was chosen arbitrarily to
543 ensure the amino acids chosen were highly similar without extracting ambiguous amino acid [64].
544 For further analysis, the results from the conservation scores were compared to each other (*i.e.,* the

545 conservation scores of ABCG5 and ABCG2 was compared to conservation scores of ABCG5 and
546 ABCG8). This was done across all comparisons to generate a comprehensive list of the amino
547 acids that are conserved across all subfamily and member combinations. The same procedure was
548 used to analyze ABCA1, ABCA7, SIDT1, SIDT2, PTCH1, and NPC1, of which experimental
549 structures have been reported [48–51].
550
551 *4.4 Homology Modelling*
552 UCSF Modeller was used for homology modelling [65]. The sequence alignment was
553 created between the template and the mutant sequences using PROMALS3D [62]. The template is
554 the currently accepted PDB ID: 5DO7 in conjunction with X-ray data to create a more accurate
555 model with a better energy DOPE (discrete optimized protein energy) score. The mutant sequences
556 included $ABCG5_{Y432F}$, $ABCG8_{N564P}$ and $ABCG5_{A540F}$. After the alignment, UCSF Modeller was
557 used to generate 400 models and to rank them based on their DOPE scores. The best model was
558 taken and visualized using PyMOL or UCSF Chimera. For the ATP-bound model, the cryo-EM
559 structure of ATP-bound ABCG2 E211Q (PDB ID: 6HBU) was used as the template [41]. 100
560 models were generated with MODELLER, and the model with the best DOPE score was used for
561 the sterol docking experiments in this study. All models were evaluated using MolProbity web
562 server [58] to ensure no severe geometric violation in the Ramachandran plot [66].
563
564 *4.5 Protein and ligand model preparation for docking*
565 Protein models ABCG1, ABCG2, ABCG5/G8, PTCH1, NPC1, ABCA1 and PDR5
566 gathered from RCSB PDB database, PDB ID: 7OZ1/7R8D, 6VXI/6VXF/6VXJ,
567 5DO7/7R8E/7JR7, 6OEU, 6UOX, 5XJY, 7P03, respectively. ABCG4, White protein, ABCA7,

568 SIDT1/2 structures were downloaded from AlphaFold2 predictions [25–27,33,34,39,48–51].
569 Regions of interest in these proteins had very high confidence scoring (pLDDT>90). Visualization
570 of the structures done through PyMOL and Chimera. Double mutant $ABCG5_{Y432F}$ and
571 $ABCG8_{N564P}$ and $ABCG5_{A540F}$ were induced and modelled in MODELLER based on PDB ID:
572 5DO7. The proteins docked (ABCG1, ABCG5/G8, ATP-bound, ABCG5/G8 mutants) were cut at
573 the elbows, excluding the nucleotide-binding domain due to the large size of the full protein (>999
574 amino acids). Cholesterol was gathered from PDB ID: 7R8D, while stigmasterol was obtained in
575 PubChem [27]. ABCG2 ligands used for docking (imatinib and SN38) were previously modelled
576 within the structure [39,40]. Dunbrack 2010 rotamer library [67] and ANTECHAMBER [68] were
577 used in dockprep charge and hydrogen bond additions.
578
579 *4.6 Molecular Docking*
580 UCSF Dock6.9 [38] was utilized through SBGrid [69] to perform molecular docking.
581 UCSF Chimera [70] was used as the graphic software for the simulated models. Protein binding
582 site was determined by "sphgen" estimation specified at 10 Å distance from the ligand, located
583 roughly in the centre of the protein in ABCG transporters. The "gridbox" and "grid" were
584 generated and analyzed prior to the dock. To avoid potential mixing-up, we first performed
585 docking with each sterol ligand on either side of transporter-membrane interface, whose results
586 were consistent with those when placing the ligands at the centre of the TMD interface. Grid was
587 built at a distance of 8 Å from the selected "sphgen" spheres, and ligand's energy was minimized
588 through minor conformational changes. A flexible docking procedure was then followed by
589 calculation of 1000 or 5000 orientations, yielding no difference in results. The best scoring poses
590 were compiled and individually viewed through UCSF Chimera's viewdock tool, these were then

591 ranked by van der Waals energy (vdw_energy) and root mean square deviation (RMSD).
592 Interacting amino acids were identified and plotted by both Chimera and PyMOL [70].
593 To validate our protocol for sterol docking on ABCG1 or ABCG5/G8, we performed a
594 control experiment using ABCG2 and three of its known drugs (i.e., imatinib, and SN38) [39].
595 Using a previously published ABCG2 structure (PDB ID: 6FFC, 6VXH and 6VXJ), ABCG2 was
596 docked with the drug ligand (one at a time) and weighed again against the originally modelled
597 pose [40]. The simulated results showed consistent orientation of the drugs between predicted and
598 experimental data, and the best pose for each drug fits the originally modelled ligand with the best
599 RMSD and the lowest van vdw_energy value. The "best pose" in this study was therefore defined
600 as the lowest van der Waal's (vdw) energy, which was used to rank all of the docking results.
601
602 *4.7 Cholesterol binding assay*
603 A direct cholesterol-binding assay using detergent-purified ABCG5/G8 was developed
604 based on the previously described [71]. Briefly, 0.24μM of His-tagged WT ABCG5/G8, the
605 mutant or the control protein (*i.e.*, BSA) was incubated with 0-4 μM of cholesterol that was
606 prepared in the presence of [^{3}H]Cholesterol with a specificity of 110cpm/fmol (Perkein Elmer) in
607 50 μl of binding buffer containing 50mM Tris-HCl pH7.5, 100mM NaCl, and 0.05%(w/v) β-DDM
608 (Anatrace), 0.05% (w/v) sodium cholate (Sigma-Aldrich), 1mM TCEP, 30μl of pre-equilibrated
609 Ni-NTA bead (QIAGEN) on ice for overnight. The supernatant was removed by centrifugation at
610 600 rpm for 1min in a bench-top centrifuge. The bead was extensively washed with 600 μl of ice-
611 cold binding buffer plus 0.01% (w/v) CHS (Steraloids) for 4 times. To elute protein, 600 μl of
612 binding buffer plus 0.01% (w/v) CHS and 200mM imidazole was added and incubated with the
613 washed bead on ice for 30min. The bound [^{3}H]Cholesterol was quantified by measuring the

614 radioactivity of 500µl of elution fraction in a liquid scintillation counter (Perkin Elmer Tri-Carb

615 4910TR).

616

617 **5. Data Availability**

618 Diffraction data have been deposited in PDB under the accession code 8CUB.

619 **AUTHOR CONTRIBUTIONS:**

620 DF carried out docking analysis of ABCG transporters and other cholesterol-binding proteins; JYL
621 performed crystallization and collected X-ray diffraction data; FR processed the X-ray data and
622 determined the crystal structure. DF, MR and AS performed sequence analysis; MR and LD
623 generated homology models. YY, JFC and JYL designed the cholesterol-binding assay; YY
624 optimized the assay and analyzed the data. JYL oversaw the project, and DF, MR, FR, SS and JYL
625 wrote the manuscript. All authors have read and agreed to the submitted version of the manuscript.

626 **FUNDING:**

627 This research was supported by a startup grant from the University of Ottawa, a Natural Sciences
628 and Engineering Research Council Discovery Grant (RGPIN 2018-04070), a National New
629 Investigator Award from the Heart and Stroke Foundation of Canada, and a Canadian Institutes of
630 Health Research Project Grant (PJT-180640) to JYL.

631 **ACKNOWLEDGEMENTS:**

632 We thank the technical help from the staff of both the Common Equipment & Technical Services
633 and the Protein Biophysics Core Facilities, as well as the critical feedback from Drs. Thomas
634 Stockner, Gregory Graf, and Ms. Annahat Kochhar. We also thank Aiman Zein, Angelica Venes
635 and Toka Hussein for technical assistance. This work is partially based on the theses that were
636 submitted to fulfill in part the requirement for the degrees of Honors Bachelor of Science (DF &
637 MR). FR is partially supported by an Academia Sinica-University of Ottawa Travel Support for
638 Research Projects. The Advanced Photon Source is a US Department of Energy Office of Science
639 User Facility operated for the Department of Energy Office of Science by Argonne National
640 Laboratory (DE-AC02-06CH11357).

641 **REFERENCES**

642 [1] W. Nan, L. Debin, C. Wengen, M. Fumihiko, T.A. R., ATP-binding cassette transporters
643 G1 and G4 mediate cellular cholesterol efflux to high-density lipoproteins, Proc. Natl.
644 Acad. Sci. 101 (2004) 9774–9779. https://doi.org/10.1073/pnas.0403506101.

645 [2] A.M. Vaughan, J.F. Oram, ABCG1 Redistributes Cell Cholesterol to Domains Removable
646 by High Density Lipoprotein but Not by Lipid-depleted Apolipoproteins *, J. Biol. Chem.
647 280 (2005) 30150–30157. https://doi.org/10.1074/jbc.M505368200.

648 [3] L. Yu, S. Gupta, F. Xu, A.D.B. Liverman, A. Moschetta, D.J. Mangelsdorf, J.J. Repa,
649 H.H. Hobbs, J.C. Cohen, Expression of ABCG5 and ABCG8 Is Required for Regulation
650 of Biliary Cholesterol Secretion *, J. Biol. Chem. 280 (2005) 8742–8747.
651 https://doi.org/10.1074/jbc.M411080200.

652 [4] D.L. Austin, Y. Weidong, A.L. V., K. Tammy, G. Yongming, R.A. K., R.D. D., A
653 multidrug resistance transporter from human MCF-7 breast cancer cells, Proc. Natl. Acad.
654 Sci. 95 (1998) 15665–15670. https://doi.org/10.1073/pnas.95.26.15665.

655 [5] J.D. Allen, A. van Loevezijn, J.M. Lakhai, M. van der Valk, O. van Tellingen, G. Reid,
656 J.H.M. Schellens, G.-J. Koomen, A.H. Schinkel, Potent and Specific Inhibition of the
657 Breast Cancer Resistance Protein Multidrug Transporter in Vitro and in Mouse Intestine
658 by a Novel Analogue of Fumitremorgin C1, Mol. Cancer Ther. 1 (2002) 417–425.

659 [6] Y. Namba, C. Sogawa, Y. Okusha, H. Kawai, M. Itagaki, K. Ono, J. Murakami, E.
660 Aoyama, K. Ohyama, J. Asaumi, M. Takigawa, K. Okamoto, S.K. Calderwood, K.
661 Kozaki, T. Eguchi, Depletion of Lipid Efflux Pump ABCG1 Triggers the Intracellular
662 Accumulation of Extracellular Vesicles and Reduces Aggregation and Tumorigenesis of
663 Metastatic Cancer Cells , Front. Oncol. . 8 (2018).

664 https://www.frontiersin.org/article/10.3389/fonc.2018.00376.
665 [7] C. Tian, D. Huang, Y. Yu, J. Zhang, Q. Fang, C. Xie, ABCG1 as a potential oncogene in
666 lung cancer, Exp Ther Med. 13 (2017) 3189–3194. https://doi.org/10.3892/etm.2017.4393.
667 [8] M.-H. Lee, K. Lu, S. Hazard, H. Yu, S. Shulenin, H. Hidaka, H. Kojima, R. Allikmets, N.
668 Sakuma, R. Pegoraro, A.K. Srivastava, G. Salen, M. Dean, S.B. Patel, Identification of a
669 gene, ABCG5, important in the regulation of dietary cholesterol absorption, Nat. Genet.
670 27 (2001) 79–83. https://doi.org/10.1038/83799.
671 [9] K.E. Berge, T. Hui, G.G. A., Y. Liqing, G.N. V., S. Joshua, K. Peter, S. Bei, B. Robert,
672 H.H. H., Accumulation of Dietary Cholesterol in Sitosterolemia Caused by Mutations in
673 Adjacent ABC Transporters, Science (80-.). 290 (2000) 1771–1775.
674 https://doi.org/10.1126/science.290.5497.1771.
675 [10] I. Meurs, B. Lammers, Y. Zhao, R. Out, R.B. Hildebrand, M. Hoekstra, T.J.C. Van
676 Berkel, M. Van Eck, The effect of ABCG1 deficiency on atherosclerotic lesion
677 development in LDL receptor knockout mice depends on the stage of atherogenesis,
678 Atherosclerosis. 221 (2012) 41–47.
679 https://doi.org/https://doi.org/10.1016/j.atherosclerosis.2011.11.024.
680 [11] T.M. Do, M.-S. Noel-Hudson, S. Ribes, C. Besengez, M. Smirnova, S. Cisternino, M.
681 Buyse, F. Calon, G. Chimini, H. Chacun, J.-M. Scherrmann, R. Farinotti, F. Bourasset,
682 ABCG2- and ABCG4-Mediated Efflux of Amyloid-β Peptide 1-40 at the Mouse Blood-
683 Brain Barrier, J. Alzheimer's Dis. 30 (2012) 155–166. https://doi.org/10.3233/JAD-2012-
684 112189.
685 [12] A.A. Zein, R. Kaur, T.O.K. Hussein, G.A. Graf, J.-Y. Lee, ABCG5/G8: a structural view
686 to pathophysiology of the hepatobiliary cholesterol secretion, Biochem. Soc. Trans. 47

687 (2019) 1259–1268. https://doi.org/10.1042/BST20190130.
688 [13] Y. Liqing, H.R. E., L.-H. Jia, von B. Klaus, L. Dieter, C.J. C., H.H. H., Disruption of
689 Abcg5 and Abcg8 in mice reveals their crucial role in biliary cholesterol secretion, Proc.
690 Natl. Acad. Sci. 99 (2002) 16237–16242. https://doi.org/10.1073/pnas.252582399.
691 [14] S.B. Patel, A. Honda, G. Salen, Sitosterolemia: exclusion of genes involved in reduced
692 cholesterol biosynthesis, J. Lipid Res. 39 (1998) 1055–1061.
693 https://doi.org/10.1016/S0022-2275(20)33874-8.
694 [15] E. Pandzic, I.C. Gelissen, R. Whan, P.J. Barter, D. Sviridov, K. Gaus, K.-A. Rye, B.J.
695 Cochran, The ATP binding cassette transporter, ABCG1, localizes to cortical actin
696 filaments, Sci. Rep. 7 (2017) 42025. https://doi.org/10.1038/srep42025.
697 [16] O. Sano, S. Ito, R. Kato, Y. Shimizu, A. Kobayashi, Y. Kimura, N. Kioka, K. Hanada, K.
698 Ueda, M. Matsuo, ABCA1, ABCG1, and ABCG4 are distributed to distinct membrane
699 meso-domains and disturb detergent-resistant domains on the plasma membrane, PLoS
700 One. 9 (2014). https://doi.org/10.1371/journal.pone.0109886.
701 [17] S. Savary, F. Denizot, M.-F. Luciani, M.-G. Mattei, G. Chimini, Molecular cloning of a
702 mammalian ABC transporter homologous to Drosophila white gene, Mamm. Genome. 7
703 (1996) 673–676. https://doi.org/10.1007/s003359900203.
704 [18] D.D. Bojanic, P.T. Tarr, G.D. Gale, D.J. Smith, D. Bok, B. Chen, S. Nusinowitz, A.
705 Lövgren-Sandblom, I. Björkhem, P.A. Edwards, Differential expression and function of
706 ABCG1 and ABCG4 during development and aging, J. Lipid Res. 51 (2010) 169–181.
707 https://doi.org/10.1194/M900250-JLR200.
708 [19] T.Q. de Aguiar Vallim, E. Lee, D.J. Merriott, C.N. Goulbourne, J. Cheng, A. Cheng, A.
709 Gonen, R.M. Allen, E.N.D. Palladino, D.A. Ford, T. Wang, Á. Baldán, E.J. Tarling,

710 ABCG1 regulates pulmonary surfactant metabolism in mice and men[S], J. Lipid Res. 58
711 (2017) 941–954. https://doi.org/https://doi.org/10.1194/jlr.M075101.
712 [20] D. Sag, C. Cekic, R. Wu, J. Linden, C.C. Hedrick, The cholesterol transporter ABCG1
713 links cholesterol homeostasis and tumour immunity, Nat. Commun. 6 (2015) 6354.
714 https://doi.org/10.1038/ncomms7354.
715 [21] G.A. Graf, L. Yu, W.-P. Li, R. Gerard, P.L. Tuma, J.C. Cohen, H.H. Hobbs, ABCG5 and
716 ABCG8 Are Obligate Heterodimers for Protein Trafficking and Biliary Cholesterol
717 Excretion*, J. Biol. Chem. 278 (2003) 48275–48282.
718 https://doi.org/https://doi.org/10.1074/jbc.M310223200.
719 [22] C. Yang, L. Yu, W. Li, F. Xu, J.C. Cohen, H.H. Hobbs, Disruption of cholesterol
720 homeostasis by plant sterols, J. Clin. Invest. 114 (2004) 813–822.
721 https://doi.org/10.1172/JCI22186.
722 [23] N. Khunweeraphong, J. Mitchell-White, D. Szöllősi, T. Hussein, K. Kuchler, I.D. Kerr, T.
723 Stockner, J.Y. Lee, Picky ABCG5/G8 and promiscuous ABCG2 - a tale of fatty diets and
724 drug toxicity, FEBS Lett. 594 (2020) 4035–4058. https://doi.org/10.1002/1873-
725 3468.13938.
726 [24] N. Khunweeraphong, D. Szöllősi, T. Stockner, K. Kuchler, The ABCG2 multidrug
727 transporter is a pump gated by a valve and an extracellular lid, Nat. Commun. 10 (2019)
728 5433. https://doi.org/10.1038/s41467-019-13302-2.
729 [25] J.Y. Lee, L.N. Kinch, D.M. Borek, J. Wang, J. Wang, I.L. Urbatsch, X.S. Xie, N. V.
730 Grishin, J.C. Cohen, Z. Otwinowski, H.H. Hobbs, D.M. Rosenbaum, Crystal structure of
731 the human sterol transporter ABCG5/ABCG8, Nature. 533 (2016) 561–564.
732 https://doi.org/10.1038/nature17666.

733 [26] L. Skarda, J. Kowal, K.P. Locher, Structure of the Human Cholesterol Transporter
734 ABCG1, J. Mol. Biol. 433 (2021) 167218.
735 https://doi.org/https://doi.org/10.1016/j.jmb.2021.167218.
736 [27] Y. Sun, J. Wang, T. Long, X. Qi, L. Donnelly, N. Elghobashi-Meinhardt, L. Esparza, J.C.
737 Cohen, X.-S. Xie, H.H. Hobbs, X. Li, Molecular basis of cholesterol efflux via ABCG
738 subfamily transporters, Proc. Natl. Acad. Sci. U. S. A. 118 (2021) e2110483118.
739 https://doi.org/10.1073/pnas.2110483118.
740 [28] M. Ristovski, D. Farhat, S.E.M. Bancud, J.-Y. Lee, Lipid Transporters Beam Signals from
741 Cell Membranes, Membranes (Basel). 11 (2021) 562.
742 https://doi.org/10.3390/membranes11080562.
743 [29] B.M. Xavier, A.A. Zein, A. Venes, J. Wang, J.Y. Lee, Transmembrane polar relay drives
744 the allosteric regulation for ABCG5/G8 sterol transporter, Int. J. Mol. Sci. 21 (2020) 1–20.
745 https://doi.org/10.3390/ijms21228747.
746 [30] Á. Telbisz, C. Özvegy-Laczka, T. Hegedűs, A. Váradi, B. Sarkadi, Effects of the lipid
747 environment, cholesterol and bile acids on the function of the purified and reconstituted
748 human ABCG2 protein, Biochem. J. 450 (2013) 387–395.
749 https://doi.org/10.1042/BJ20121485.
750 [31] G. Gimpl, Interaction of G protein coupled receptors and cholesterol, Chem. Phys. Lipids.
751 199 (2016) 61–73. https://doi.org/10.1016/j.chemphyslip.2016.04.006.
752 [32] D. Xu, Y. Li, F. Yang, C.-R. Sun, J. Pan, L. Wang, Z.-P. Chen, S.-C. Fang, X. Yao, W.-T.
753 Hou, C.-Z. Zhou, Y. Chen, Structure and transport mechanism of the human cholesterol
754 transporter ABCG1, Cell Rep. 38 (2022) 110298.
755 https://doi.org/https://doi.org/10.1016/j.celrep.2022.110298.

[33] H. Zhang, C.-S. Huang, X. Yu, J. Lee, A. Vaish, Q. Chen, M. Zhou, Z. Wang, X. Min, Cryo-EM structure of ABCG5/G8 in complex with modulating antibodies, Commun. Biol. 4 (2021) 526. https://doi.org/10.1038/s42003-021-02039-8.

[34] A. Harris, M. Wagner, D. Du, S. Raschka, L.-M. Nentwig, H. Gohlke, S.H.J. Smits, B.F. Luisi, L. Schmitt, Structure and efflux mechanism of the yeast pleiotropic drug resistance transporter Pdr5, Nat. Commun. 12 (2021) 5254. https://doi.org/10.1038/s41467-021-25574-8.

[35] M.J. Ferreiro, C. Pérez, M. Marchesano, S. Ruiz, A. Caputi, P. Aguilera, R. Barrio, R. Cantera, Drosophila melanogaster White Mutant w(1118) Undergo Retinal Degeneration, Front. Neurosci. 11 (2018) 732. https://doi.org/10.3389/fnins.2017.00732.

[36] Y. Mahé, Y. Lemoine, K. Kuchler, The ATP Binding Cassette Transporters Pdr5 and Snq2 of Saccharomyces cerevisiae Can Mediate Transport of Steroids in Vivo*, J. Biol. Chem. 271 (1996) 25167–25172. https://doi.org/10.1074/jbc.271.41.25167.

[37] L. Yu, K. von Bergmann, D. Lutjohann, H.H. Hobbs, J.C. Cohen, Selective sterol accumulation in ABCG5/ABCG8-deficient mice, J. Lipid Res. 45 (2004) 301–307. https://doi.org/10.1194/jlr.M300377-JLR200.

[38] W.J. Allen, T.E. Balius, S. Mukherjee, S.R. Brozell, D.T. Moustakas, P.T. Lang, D.A. Case, I.D. Kuntz, R.C. Rizzo, DOCK 6: Impact of new features and current docking performance, J. Comput. Chem. 36 (2015) 1132–1156. https://doi.org/10.1002/jcc.23905.

[39] B.J. Orlando, M. Liao, ABCG2 transports anticancer drugs via a closed-to-open switch, Nat. Commun. 11 (2020) 2264. https://doi.org/10.1038/s41467-020-16155-2.

[40] S.M. Jackson, I. Manolaridis, J. Kowal, M. Zechner, N.M.I. Taylor, M. Bause, S. Bauer,

779 R. Bartholomaeus, G. Bernhardt, B. Koenig, A. Buschauer, H. Stahlberg, K.-H. Altmann,
780 K.P. Locher, Structural basis of small-molecule inhibition of human multidrug transporter
781 ABCG2, Nat. Struct. Mol. Biol. 25 (2018) 333–340. https://doi.org/10.1038/s41594-018-
782 0049-1.
783 [41] I. Manolaridis, S.M. Jackson, N.M.I. Taylor, J. Kowal, H. Stahlberg, K.P. Locher, Cryo-
784 EM structures of a human ABCG2 mutant trapped in ATP-bound and substrate-bound
785 states, Nature. 563 (2018) 426–430. https://doi.org/10.1038/s41586-018-0680-3.
786 [42] D. Sehnal, R. Svobodová Vařeková, K. Berka, L. Pravda, V. Navrátilová, P. Banáš, C.-M.
787 Ionescu, M. Otyepka, J. Koča, MOLE 2.0: advanced approach for analysis of
788 biomacromolecular channels., J. Cheminform. 5 (2013) 39. https://doi.org/10.1186/1758-
789 2946-5-39.
790 [43] A.I. Greenwood, S. Tristram-Nagle, J.F. Nagle, Partial molecular volumes of lipids and
791 cholesterol., Chem. Phys. Lipids. 143 (2006) 1–10.
792 https://doi.org/10.1016/j.chemphyslip.2006.04.002.
793 [44] Q. Yu, D. Ni, J. Kowal, I. Manolaridis, S.M. Jackson, H. Stahlberg, K.P. Locher,
794 Structures of ABCG2 under turnover conditions reveal a key step in the drug transport
795 mechanism, Nat. Commun. 12 (2021) 4376. https://doi.org/10.1038/s41467-021-24651-2.
796 [45] N.M.I. Taylor, I. Manolaridis, S.M. Jackson, J. Kowal, H. Stahlberg, K.P. Locher,
797 Structure of the human multidrug transporter ABCG2, Nature. 546 (2017) 504–509.
798 https://doi.org/10.1038/nature22345.
799 [46] T. Gose, T. Shafi, Y. Fukuda, S. Das, Y. Wang, A. Allcock, A. Gavan McHarg, J. Lynch,
800 T. Chen, I. Tamai, A. Shelat, R.C. Ford, J.D. Schuetz, ABCG2 requires a single aromatic
801 amino acid to “clamp” substrates and inhibitors into the binding pocket, FASEB J. 34

802 (2020) 4890–4903. https://doi.org/10.1096/fj.201902338RR.
803 [47] T. Nagy, Á. Tóth, Á. Telbisz, B. Sarkadi, H. Tordai, A. Tordai, T. Hegedűs, The transport
804 pathway in the ABCG2 protein and its regulation revealed by molecular dynamics
805 simulations, Cell. Mol. Life Sci. 78 (2021) 2329–2339. https://doi.org/10.1007/s00018-
806 020-03651-3.
807 [48] H. Qian, X. Zhao, P. Cao, J. Lei, N. Yan, X. Gong, Structure of the Human Lipid Exporter
808 ABCA1, Cell. 169 (2017) 1228-1239.e10. https://doi.org/10.1016/j.cell.2017.05.020.
809 [49] X. Qi, P. Schmiege, E. Coutavas, J. Wang, X. Li, Structures of human Patched and its
810 complex with native palmitoylated sonic hedgehog, Nature. 560 (2018) 128–132.
811 https://doi.org/10.1038/s41586-018-0308-7.
812 [50] T. Long, X. Qi, A. Hassan, Q. Liang, J.K. De Brabander, X. Li, Structural basis for
813 itraconazole-mediated NPC1 inhibition, Nat. Commun. 11 (2020) 152.
814 https://doi.org/10.1038/s41467-019-13917-5.
815 [51] J. Jumper, R. Evans, A. Pritzel, T. Green, M. Figurnov, O. Ronneberger, K.
816 Tunyasuvunakool, R. Bates, A. Žídek, A. Potapenko, A. Bridgland, C. Meyer, S.A.A.
817 Kohl, A.J. Ballard, A. Cowie, B. Romera-Paredes, S. Nikolov, R. Jain, J. Adler, T. Back,
818 S. Petersen, D. Reiman, E. Clancy, M. Zielinski, M. Steinegger, M. Pacholska, T.
819 Berghammer, S. Bodenstein, D. Silver, O. Vinyals, A.W. Senior, K. Kavukcuoglu, P.
820 Kohli, D. Hassabis, Highly accurate protein structure prediction with AlphaFold, Nature.
821 596 (2021) 583–589. https://doi.org/10.1038/s41586-021-03819-2.
822 [52] O. Sano, A. Kobayashi, K. Nagao, K. Kumagai, N. Kioka, K. Hanada, K. Ueda, M.
823 Matsuo, Sphingomyelin-dependence of cholesterol efflux mediated by ABCG1, J. Lipid
824 Res. 48 (2007) 2377–2384. https://doi.org/10.1194/jlr.M700139-JLR200.

825 [53] I. Ermilova, A.P. Lyubartsev, Cholesterol in phospholipid bilayers: positions and
826 orientations inside membranes with different unsaturation degrees, Soft Matter. 15 (2019)
827 78–93. https://doi.org/10.1039/C8SM01937A.
828 [54] Z. Otwinowski, W.B.T.-M. in E. Minor, [20] Processing of X-ray diffraction data
829 collected in oscillation mode, in: Macromol. Crystallogr. Part A, Academic Press, 1997:
830 pp. 307–326. https://doi.org/https://doi.org/10.1016/S0076-6879(97)76066-X.
831 [55] M.J. Grayling, PhaseR: An R package for phase plane analysis of autonomous ODE
832 systems, R J. 6 (2014) 43–51. https://doi.org/10.32614/rj-2014-023.
833 [56] P.D. Adams, P. V Afonine, G. Bunkóczi, V.B. Chen, I.W. Davis, N. Echols, J.J. Headd,
834 L.-W. Hung, G.J. Kapral, R.W. Grosse-Kunstleve, A.J. McCoy, N.W. Moriarty, R.
835 Oeffner, R.J. Read, D.C. Richardson, J.S. Richardson, T.C. Terwilliger, P.H. Zwart,
836 PHENIX: a comprehensive Python-based system for macromolecular structure solution,
837 Acta Crystallogr. D. Biol. Crystallogr. 66 (2010) 213–221.
838 https://doi.org/10.1107/S0907444909052925.
839 [57] P. Emsley, K. Cowtan, {\it Coot}: model-building tools for molecular graphics, Acta
840 Crystallogr. Sect. D. 60 (2004) 2126–2132. https://doi.org/10.1107/S0907444904019158.
841 [58] V.B. Chen, W.B. Arendall 3rd, J.J. Headd, D.A. Keedy, R.M. Immormino, G.J. Kapral,
842 L.W. Murray, J.S. Richardson, D.C. Richardson, MolProbity: all-atom structure validation
843 for macromolecular crystallography, Acta Crystallogr. D. Biol. Crystallogr. 66 (2010) 12–
844 21. https://doi.org/10.1107/S0907444909042073.
845 [59] P.J.A. Cock, T. Antao, J.T. Chang, B.A. Chapman, C.J. Cox, A. Dalke, I. Friedberg, T.
846 Hamelryck, F. Kauff, B. Wilczynski, M.J.L. de Hoon, Biopython: freely available Python
847 tools for computational molecular biology and bioinformatics, Bioinformatics. 25 (2009)

848 1422–1423. https://doi.org/10.1093/bioinformatics/btp163.
849 [60] S. Henikoff, J.G. Henikoff, Amino acid substitution matrices from protein blocks, Proc.
850 Natl. Acad. Sci. U. S. A. 89 (1992) 10915–10919.
851 https://doi.org/10.1073/pnas.89.22.10915.
852 [61] J.D. Thompson, D.G. Higgins, T.J. Gibson, CLUSTAL W: improving the sensitivity of
853 progressive multiple sequence alignment through sequence weighting, position-specific
854 gap penalties and weight matrix choice, Nucleic Acids Res. 22 (1994) 4673–4680.
855 https://doi.org/10.1093/nar/22.22.4673.
856 [62] J. Pei, B.-H. Kim, N. V Grishin, PROMALS3D: a tool for multiple protein sequence and
857 structure alignments, Nucleic Acids Res. 36 (2008) 2295–2300.
858 https://doi.org/10.1093/nar/gkn072.
859 [63] R.C. Edgar, MUSCLE: multiple sequence alignment with high accuracy and high
860 throughput, Nucleic Acids Res. 32 (2004) 1792–1797. https://doi.org/10.1093/nar/gkh340.
861 [64] C.D. Livingstone, G.J. Barton, Protein sequence alignments: a strategy for the hierarchical
862 analysis of residue conservation, Bioinformatics. 9 (1993) 745–756.
863 https://doi.org/10.1093/bioinformatics/9.6.745.
864 [65] B. Webb, A. Sali, Protein Structure Modeling with MODELLER BT - Protein Structure
865 Prediction, in: D. Kihara (Ed.), Springer New York, New York, NY, 2014: pp. 1–15.
866 https://doi.org/10.1007/978-1-4939-0366-5_1.
867 [66] C.J. Williams, J.J. Headd, N.W. Moriarty, M.G. Prisant, L.L. Videau, L.N. Deis, V.
868 Verma, D.A. Keedy, B.J. Hintze, V.B. Chen, S. Jain, S.M. Lewis, W.B. Arendall 3rd, J.
869 Snoeyink, P.D. Adams, S.C. Lovell, J.S. Richardson, D.C. Richardson, MolProbity: More
870 and better reference data for improved all-atom structure validation, Protein Sci. 27 (2018)

871 293–315. https://doi.org/10.1002/pro.3330.
872 [67] M. V Shapovalov, R.L. Dunbrack Jr, A smoothed backbone-dependent rotamer library
873 for proteins derived from adaptive kernel density estimates and regressions, Structure. 19
874 (2011) 844–858. https://doi.org/10.1016/j.str.2011.03.019.
875 [68] J. Wang, W. Wang, P.A. Kollman, D.A. Case, Automatic atom type and bond type
876 perception in molecular mechanical calculations, J. Mol. Graph. Model. 25 (2006) 247–
877 260. https://doi.org/https://doi.org/10.1016/j.jmgm.2005.12.005.
878 [69] A. Morin, B. Eisenbraun, J. Key, P.C. Sanschagrin, M.A. Timony, M. Ottaviano, P. Sliz,
879 Collaboration gets the most out of software, Elife. 2 (2013) e01456.
880 https://doi.org/10.7554/eLife.01456.
881 [70] E.F. Pettersen, T.D. Goddard, C.C. Huang, G.S. Couch, D.M. Greenblatt, E.C. Meng, T.E.
882 Ferrin, UCSF Chimera - A visualization system for exploratory research and analysis, J.
883 Comput. Chem. 25 (2004) 1605–1612. https://doi.org/10.1002/jcc.20084.
884 [71] A. Radhakrishnan, L.-P. Sun, H.J. Kwon, M.S. Brown, J.L. Goldstein, Direct Binding of
885 Cholesterol to the Purified Membrane Region of SCAP: Mechanism for a Sterol-Sensing
886 Domain, Mol. Cell. 15 (2004) 259–268. https://doi.org/10.1016/j.molcel.2004.06.019.
887

888 **Table 1: Crystallographic data collection and refinement.**

Beamline	APS 19-ID
Number of crystals	3
Wavelength	0.9794
Resolution range	30.58 - 4.051 (4.195 - 4.051)*
Space group	I 2 2 2
Unit cell (*a, b, c* (Å))	173.268 230.11 249.819 90 90 90
Total reflections	427824 (30232)
Unique reflections	38173 (915)
Multiplicity	11.2 (14.4)
Completeness (%)	83.96 (22.75)
Mean I/sigma(I)	5.90 (1.41)
R-merge	3.392 (5.094)
CC1/2	0.377 (0.137)
CC*	0.74 (0.491)
Reflections used in refinement	34374 (915)
Reflections used for R-free	2016 (54)
R-work	0.2459 (0.2832)
R-free	0.3029 (0.3039)
CC(work)	0.864 (0.703)
CC(free)	0.817 (0.715)
Number of non-hydrogen atoms	18498

macromolecules	18442
ligands	56
RMS(bonds)	0.005
RMS(angles)	0.93
Ramachandran favored (%)	93.54
Ramachandran allowed (%)	5.90
Ramachandran outliers (%)	0.56
Rotamer outliers (%)	0.00
Clashscore	11.97
Average B-factor	52.45
macromolecules	52.45
ligands	49.48
Number of TLS groups	1

* Statistics for the highest-resolution shell are shown in parentheses.

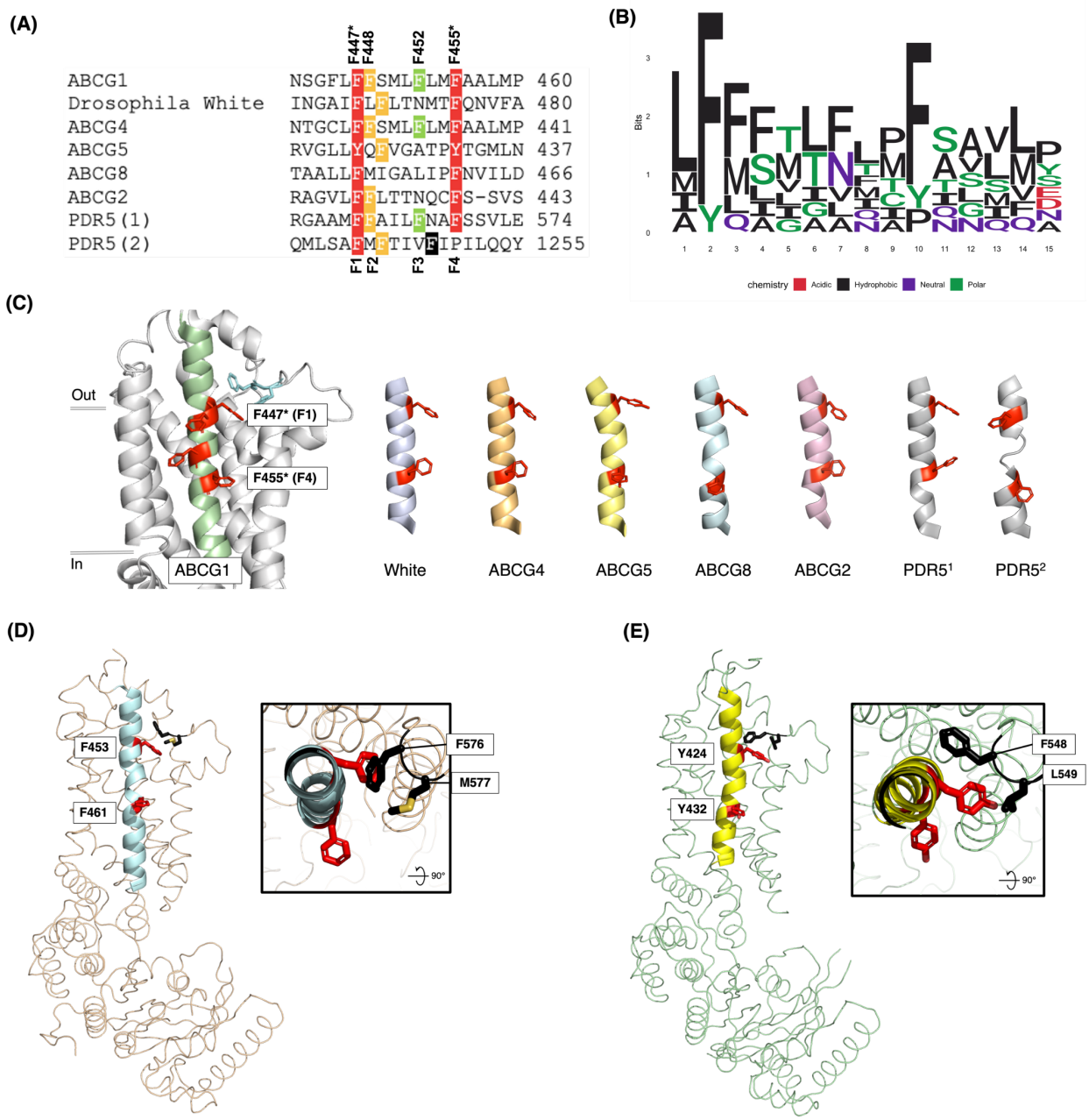

Figure 1. Conservation of aromatic amino acids on TMH2 of human ABCG family protein and homologues, including their localization in relation to key regions in the ABCG5/G8 heterodimer. (A) Sequence analysis of transmembrane helix five (TMH2) was done through PROMALS3D. Residues were screened for high conservation through BLAST sequence analysis. Red highlights perfect (or near perfect) aromatic residue conservation. Orange highlights conservation with ± 1 residue displacement. Green shows moderate conservation. Black shows non-sequence, but rather structural conservation. **(B)** Logo plot of TMH2 residues are colored according to their chemical nature. Red: acidic amino acids; Black: hydrophobic amino acids; Purple: neutral residues; Green: polar residues. **(C)** Structural conservation of highlighted aromatic amino acids from (A), using ABCG1 amino acid numeration as a reference. ABCG1 (PDB ID: 7OZ1, green), ABCG2 (PDB ID: 6VXI, pink, ABCG5/G8 (PDB ID: 5DO7; G5 in blue, G8 in

903 yellow), PDR5-1 and 2 (PDB ID: 7PO3, light grey). *Drosophila* White (purple) and ABCG4
904 (orange) are the only two Alphafold models, both have helices with predicted local distance
905 difference test score of >90. F447 (F1) and F455 (F4) residues in relation to ABCG1, have the
906 highest conservation. The residues directions are maintained, with F447 stacking under the
907 hydrophobic valve and F455 pointing towards the lumenal space between the TMD dimer. ABCG5
908 is the only monomer which has tyrosine's instead of phenylalanine's. ABCG1 and ABCG4 have
909 large hydrophobic amino acids pointing lumenally causing a mass hydrophobic region spanning
910 most of the transmembrane domain. **(D, E)** ABCG5/G8 heterodimer is split and shown in a top-
911 down view, highlighting the location of conserved F453 and Y424 (red) in relation to hydrophobic
912 valves (black). **(D)** In ABCG8, F453 (F1) stacks underneath F576, which (along M577) comprise
913 the hydrophobic valve shown in black. **(E)** In ABCG5, Y424 (F1) is stacked underneath both
914 hydrophobic valve residues; F548 and L549, shown in black.

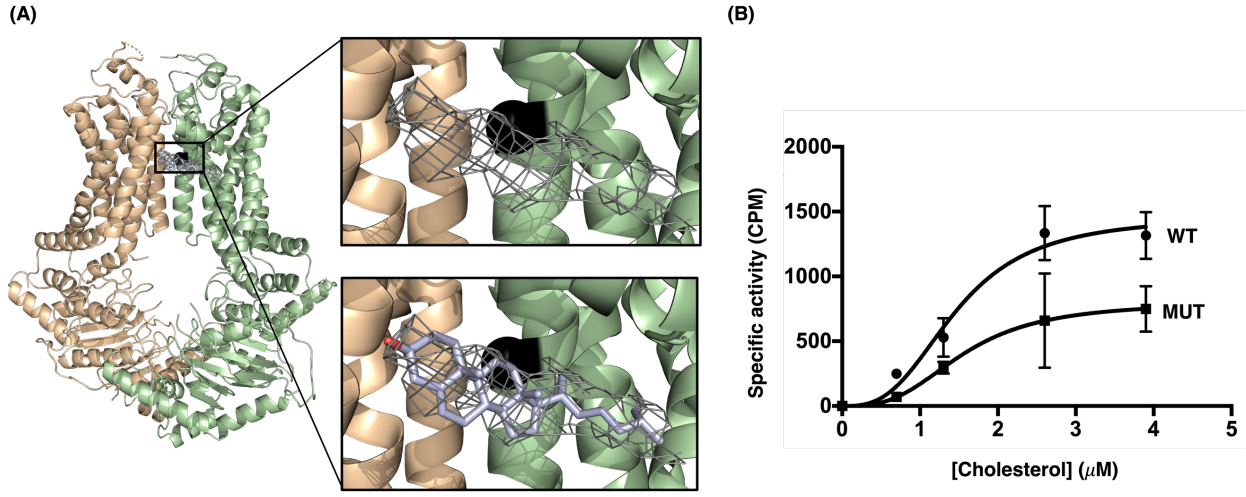

Figure 2. Crystal structure of cholesterol-bound ABCG5/G8 and cholesterol-binding assay. (A) Cholesterol-bound ABCG5/G8 structure is plotted in cartoon presentation. The first zoomed-in picture shows the electron density related to the cholesterol molecule which was observed at the interface of transmembrane domains of the crystallographic dimers (top right). The cholesterol molecule was modeled to the primary structure as shown in the second zoomed-in picture (bottom right). Alanine 540 (A540) is marked in a black sphere as a residue involved in the cholesterol-binding site. **(B)** The cholesterol-binding activities of the WT and the A540F mutant were measured by using [^{3}H]-cholesterol, showing the binding parameters for the WT and the mutant with Bmax = 50.64±0.77 and 27.65±0.01 μCi/ml, K_D = 1.46 ±0.28 and 1.55±0.01 μM, and h = 2.91 and 2.98, respectively. A P-value = 0.043 was obtained by paired t-test between WT and mutant. All calculations were performed using GraphPad Prism programs.

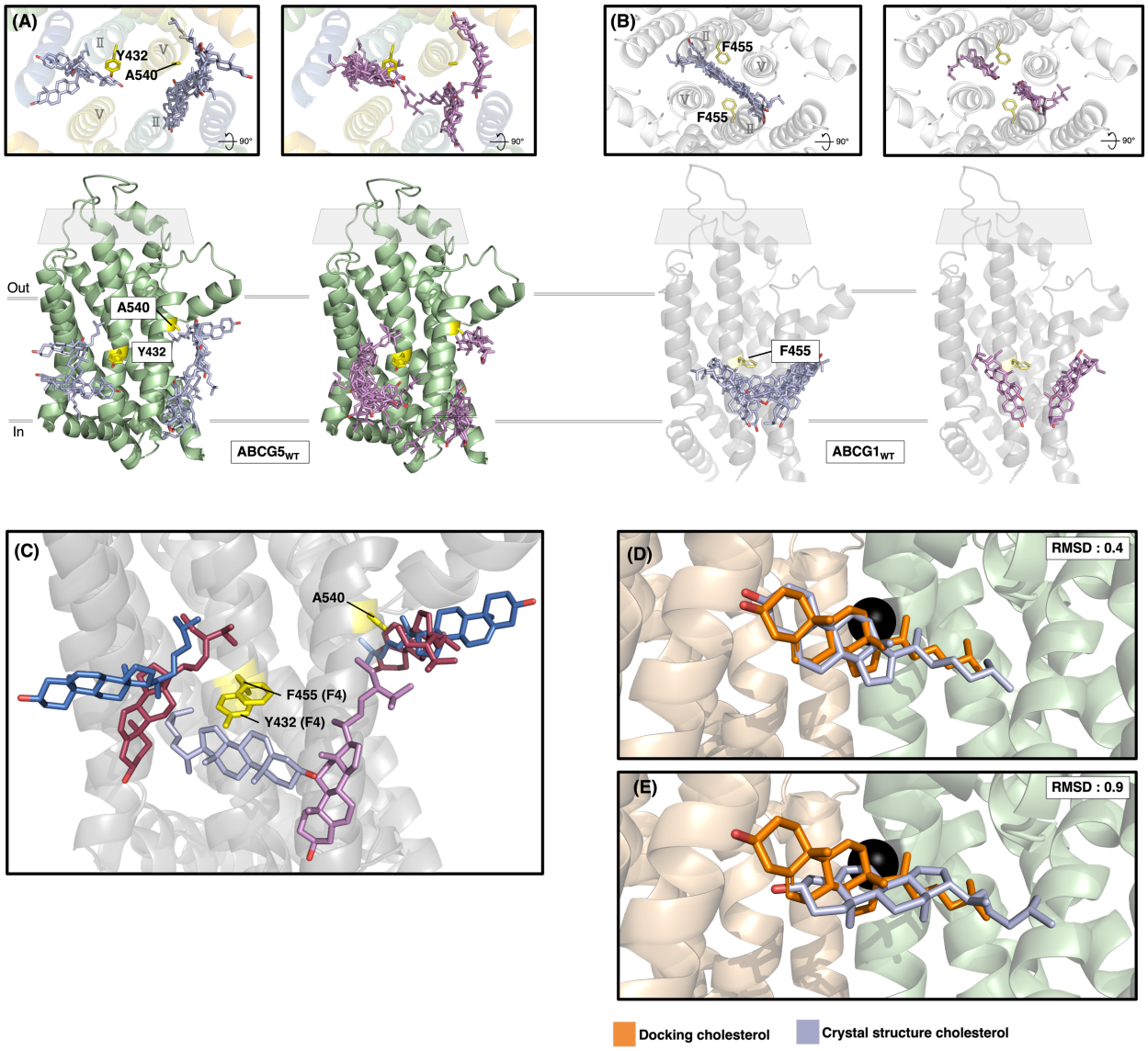

Figure 3. Cholesterol and stigmasterol docking in ABCG5/G8 and ABCG1. (A-B) Cholesterol (blue, left) and stigmasterol (violet, right) are bound to either side of the interface between the two dimers. TMH2 and TMH5 are labeled as II and V. **(A)** Cholesterol or stigmasterol in ABCG5/G8 docks differently on either side (shown only ABCG5 here). *Left of Y432*, cholesterol docks in three conformations: lightly angled upwards above Y432, horizontal on the X-axis below Y432 and vertical. Stigmasterol (right) poses to the left of Y432 has a "C" shaped pattern that surrounds Y432. *Right of Y432*, cholesterol binds in a continuous pattern, starting at A540 and ending at the lower edge of the transmembrane domain (TMD). A single cholesterol conformation binds horizontally near A540. Stigmasterol binds in two separated clusters with the top cluster showing horizontal poses ahead of A540 and the bottom cluster containing horizontally oriented sterols. **(B)** On ABCG1 (PDB ID: 7OZ1), either cholesterol or stigmasterol includes similar docking poses on both sides. The sterols are angled towards the putative sterol binding cavity on the cytoplasmic end of the bilayers. Given similar binding pattern, more cholesterol poses are obtained than stigmasterol. **(C)** Top sterol poses on both transporters are illustrated as a superposition**.** ABCG1 cholesterol and stigmasterol are colored blue and violet respectively. ABCG5/G8 cholesterol and stigmasterol are colored dark blue and dark red respectively. In general, sterols in ABCG5/G8

944 dock higher, near the orthogonal sterol-binding site, whereas sterols in ABCG1 binds under F455
945 (below F4 of the phenylalanine highway). **(D, E)** The cholesterol docking pose (orange) is aligned
946 with either cholesterol in the asymmetric unit of the crystal structure (light blue) with an RMSD
947 of 0.4 Å (D) and 0.9 Å (E).

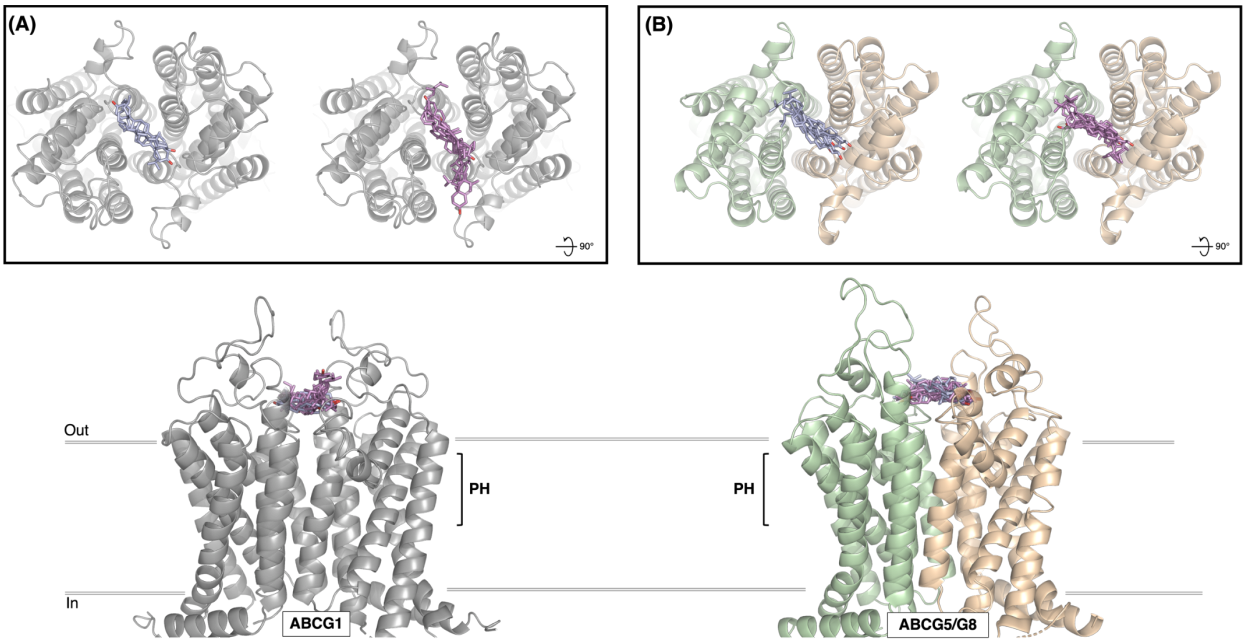

Figure 4. (A, B) Sterol docking on ATP-bound ABCG1 (A) and ABCG5/G8 (B) models. ABCG1 (PDB ID: 7R8E) in gray; ABCG5/G8 in pale-green and tan. Cholesterol (blue) and stigmasterol (violet) docked shown in a front view (lower) and a top-down view (upper). In brackets is the extent of the phenylalanine highway (PH) within the transmembrane domain (TMD) of the protein.

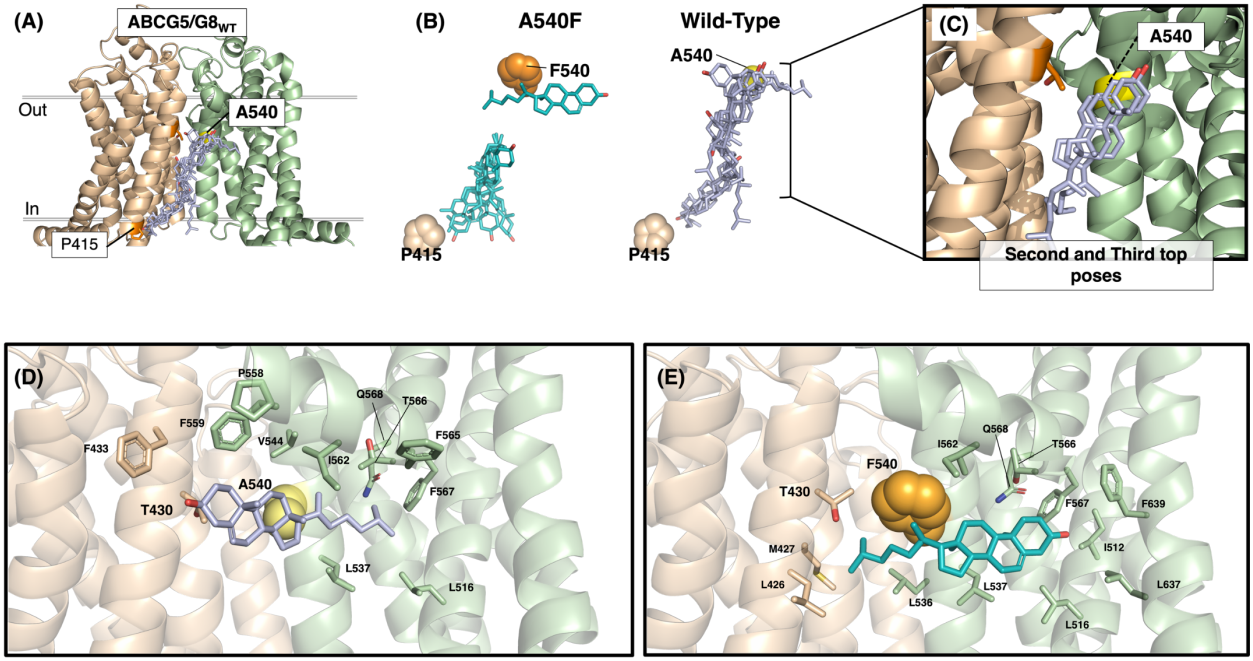

Figure 5. Wild-type and mutant A540F ABCG5/G8 docking predictions. (A-C) ABCG5 and ABCG8 are colored in pale-green and tan respectively, and the cholesterol docking on WT results are shown in (A). In comparison, WT docking is shown in blue while mutant is shown in teal (B). Landmark residues $ABCG5_{A540}$ and $ABCG8_{P415}$ are highlighted in tan and orange respectively for the orientation (B), showing that WT has a continuous cholesterol binding pattern from A540 to P415 while the mutant has a break in the docking prediction, separating the two clusters. Two of the top 3 poses in the wild type docking appear to be missing in the A540F mutant (C). **(D, E)** The micro-environment surrounding cholesterol highlights sterol-protein interaction. Residues are shown as sticks. From left to right, ABCG8: L426, M427, T430; ABCG5: F559, F540, L536, I562, L537 Q568, T566, F567, L516, L637. The side chain of F540 is shown in spheres to highlight the mutation.

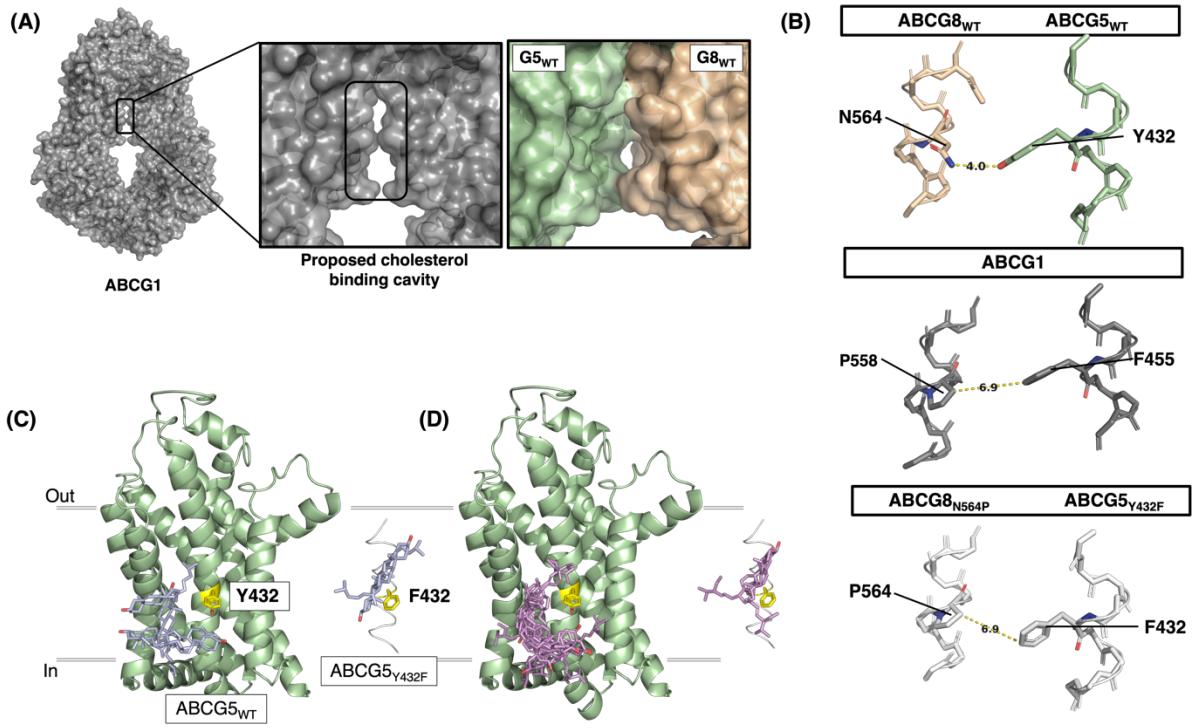

Figure 6. Lower transmembrane cavity in ABCG5/G8 and ABCG1 with cholesterol and stigmasterol docking on wild-type and double mutant (Y432F, N564P) ABCG5/G8. (A) ABCG1's (PDB ID: 7OZ1, gray) hollow transmembrane region was previously denoted as a putative cholesterol binding cavity contrasted with ABCG5 (pale-green)/G8(tan). All atoms are included (but not displayed) with the surface fit over the protein. **(B)** WT ABCG5/G8 (PDB ID: 7RJ7, pale-green/tan) with residues Y432 and N564 shown as sticks. Distance between the two amino acids is ~4.0 Å, and for the equivalent residues in ABCG1 (PDB ID: 7OZ1, gray), F455 and P558, they are ~6.9 Å apart. A homology model of the double-mutant ABCG5/G8, shown in white, has Y432 and N564 substituted for phenylalanine and proline, respectively, as observed in ABCG1. **(C, D)** Cholesterol (blue) and stigmasterol (violet) docking was simulated on WT and double mutant (white) ABCG5/G8, with only ABCG5 shown here. Yellow: residue 432 on ABCG5. Wild type has more potential binding poses than the double mutant that only binds a handful sterols above residue 432.

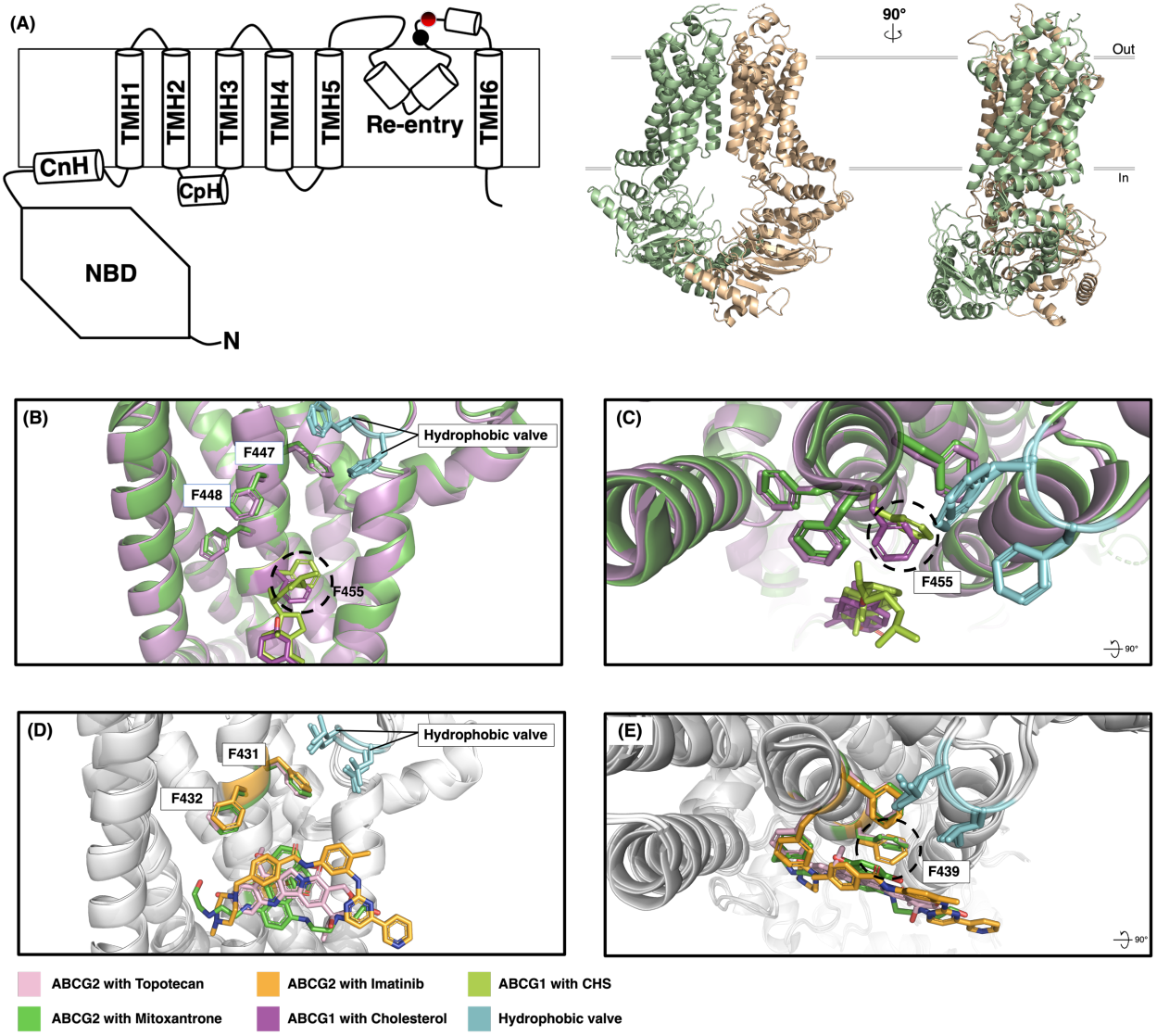

Supplemental Figure 1. Topological representation of the ABCG5/G8 and Superposition of the phenylalanine highway on ABCG1 and ABCG2. (A) *Left,* Topological representation of the ABCG5/G8 crystal structure (PDB ID: 8CUB) is depicted in empty cylinders, showing the transmembrane structural segments of ABCG5/G8 including connecting helixes (CnH), TM helixes, coupling helices (CpH), and re-entry helixes. *Right,* The cartoon illustration of the ABCG5/G8 heterodimer with ABCG5 in pale-green and ABCG8 in tan colors. The N-glycosylation sites are shown in solid circles: $ABCG5_{N592}$ or $ABCG8_{N619}$ in red and black, $ABCG5_{N584}$ in black. **(B)** Side view of ABCG1 (PDB ID: 7OZ1), showing the difference in height of CHS (green) and cholesterol (purple). **(C)** Top-down view ABCG1 bound to CHS (PDB ID: 7OZ1, green) aligned with ABCG1 bound to cholesterol (7R8D, purple) emphasizing the difference in F455 rotation when interacting with different length ligands. Rotation occurs when longer ligands (such as CHS) reach deep enough into the transmembrane cavity, causing the alpha carbon and phenyl side chain of F455 to rotate. F447 is also seen stacked under hydrophobic valve. **(D)** Side view of ABCG2, showing the difference in localization of Imatinib (orange), Topotecan (pink), Mitoxantrone (green). **(E)**Top-down view of ABCG2 bound with Imatinib (PDB ID:

6VXH, orange), Topotecan (PDB ID :6VXJ, pink) and Mitoxantrone (PDB ID: 6VXI, green). Rotation of F439 is seen when substrates are deep enough into the cavity to interact with the residue. Contrarily, when they are not, such rotation events do not happen, as observed with Imatinib.

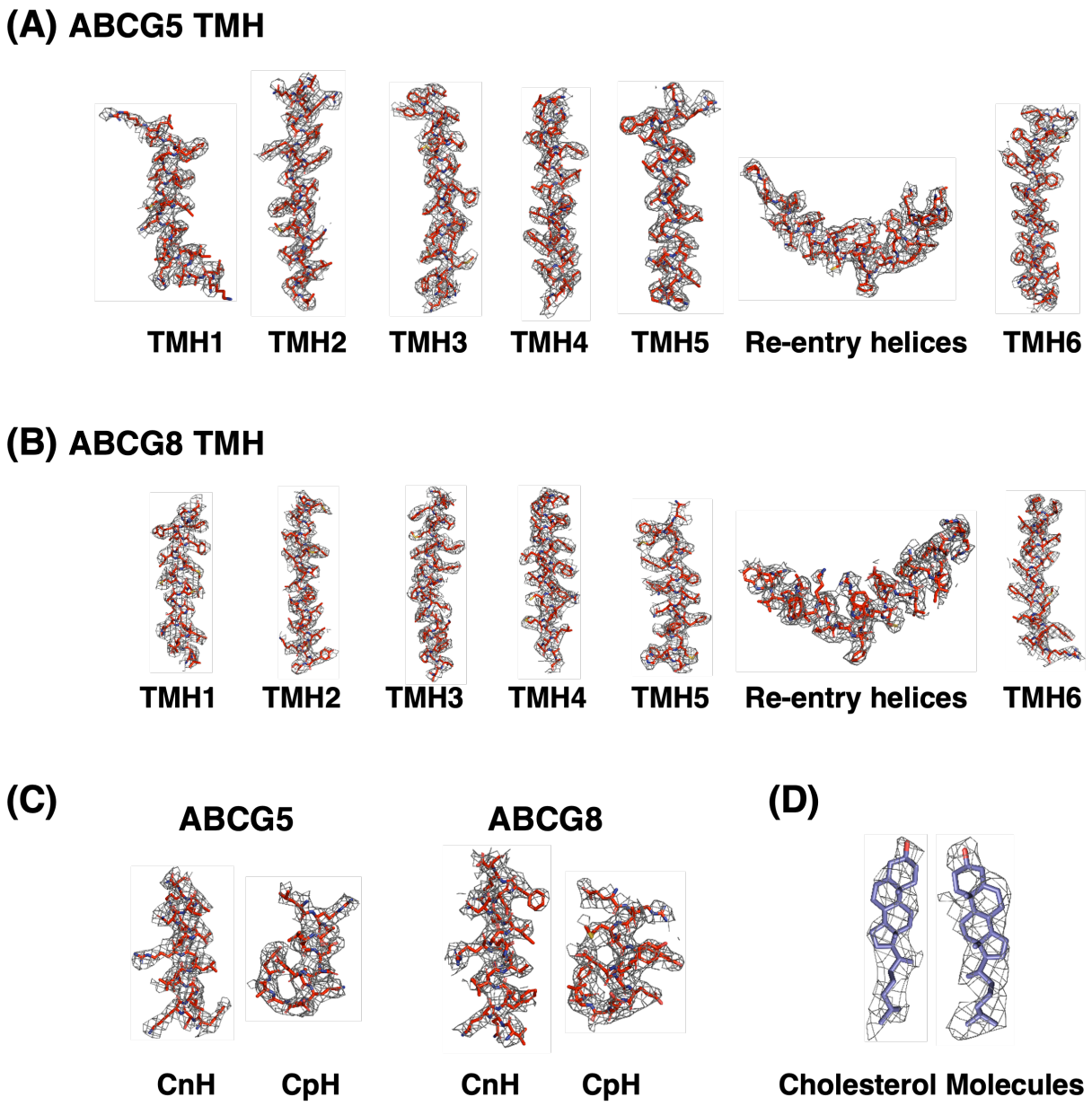

Supplemental Figure 2. The fitting of the structural model in the electron densities (2Fo-Fc omit map). The representative segments of the human ABCG5/G8 proteins, including transmembrane (A/B), connecting (C), coupling helixes (C), and cholesterol molecules (D) are shown separately for G5 and G8 chains in the electron density with a mesh contoured at 1 σ and the thickness of 1.5 as implemented in PyMOL.

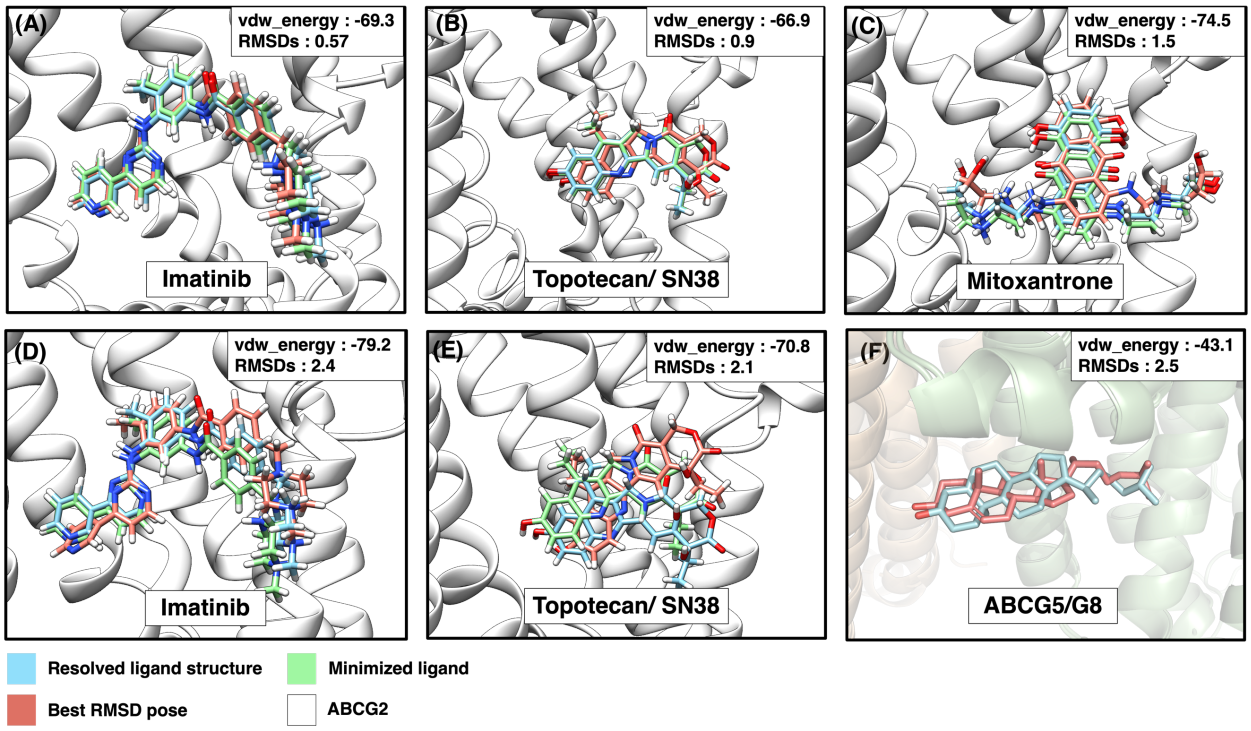

Supplemental Figure 3. Resolved ligand structures compared to dock prediction in ABCG2 (A-E) and ABCG5/G8 (F). (**A-C**) **Redocking of** resolved ligands on ABCG2 (blue): Topotecan/SN38 (PDB ID :6VXJ), Mitoxantrone (PDB ID: 6VXI), and Imatinib (PDB ID: 6VXH). Green highlights the minimized rigid conformation as calculated by Dock6.9. Orange highlights the best predicted pose. Blue ligands were observed in the experimentally determined structures. RMSD of all superpositions is (0.57Å – 1.5Å). (**D**/**E**) Ligands were aligned and docked to ABCG2 (PDB ID: 6FFC). Pink highlights the best RMSD predicted pose. The RMSD of all superpositions is (2.1Å – 2.4Å). (**F**) Redocking of cholesterol ligand on ABCG5/G8 (RMSD 2.5Å, present study). See details in Materials and Methods.

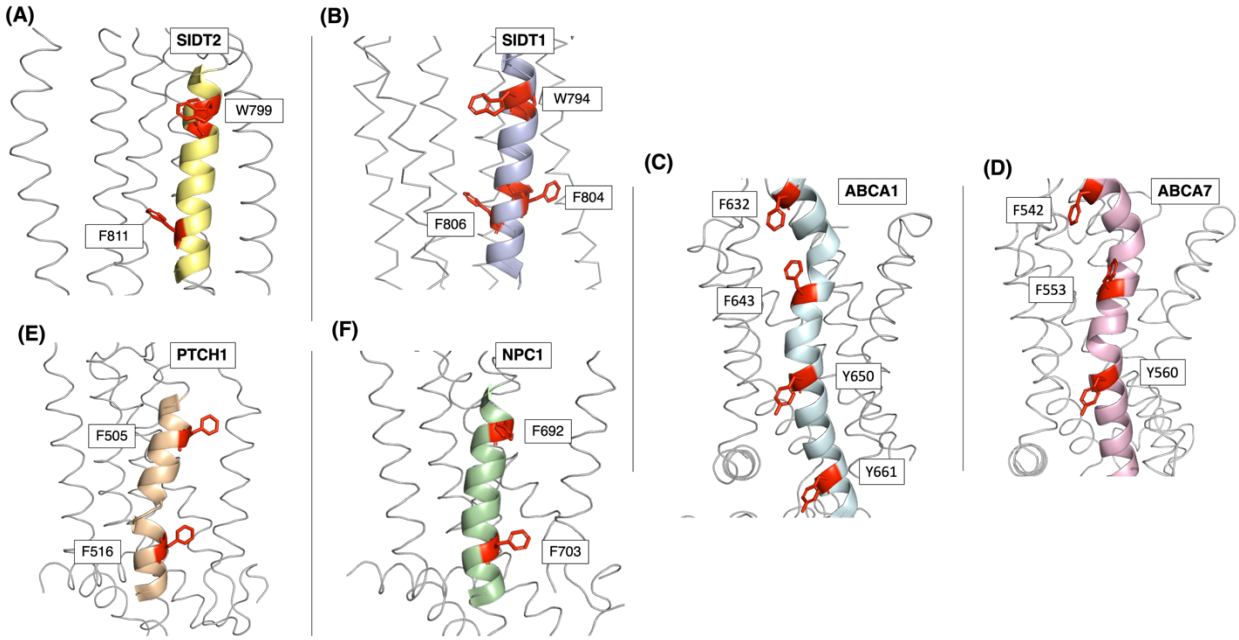

Supplemental Figure 4. Aromatic amino acid pattern in non-ABCG lipid transporters. Conserved aromatic residues along the putative (or observed) sterol-binding/interacting TMH (cartoon presentation) show a similar pattern of phenylalanine highway as observed in ABCG transporters. SIDT2 (**A**, yellow), SIDT1 (**B**, dark blue), ABCA1 (**C**, light blue), ABCA7 (**D**, pink), PTCH1 (**E**, orange) and NPC1 (**F**, green). The aromatic amino acids: phenylalanine, tyrosine and tryptophan are highlighted in red sticks. Only the most central and luminal helices are modelled in detail.

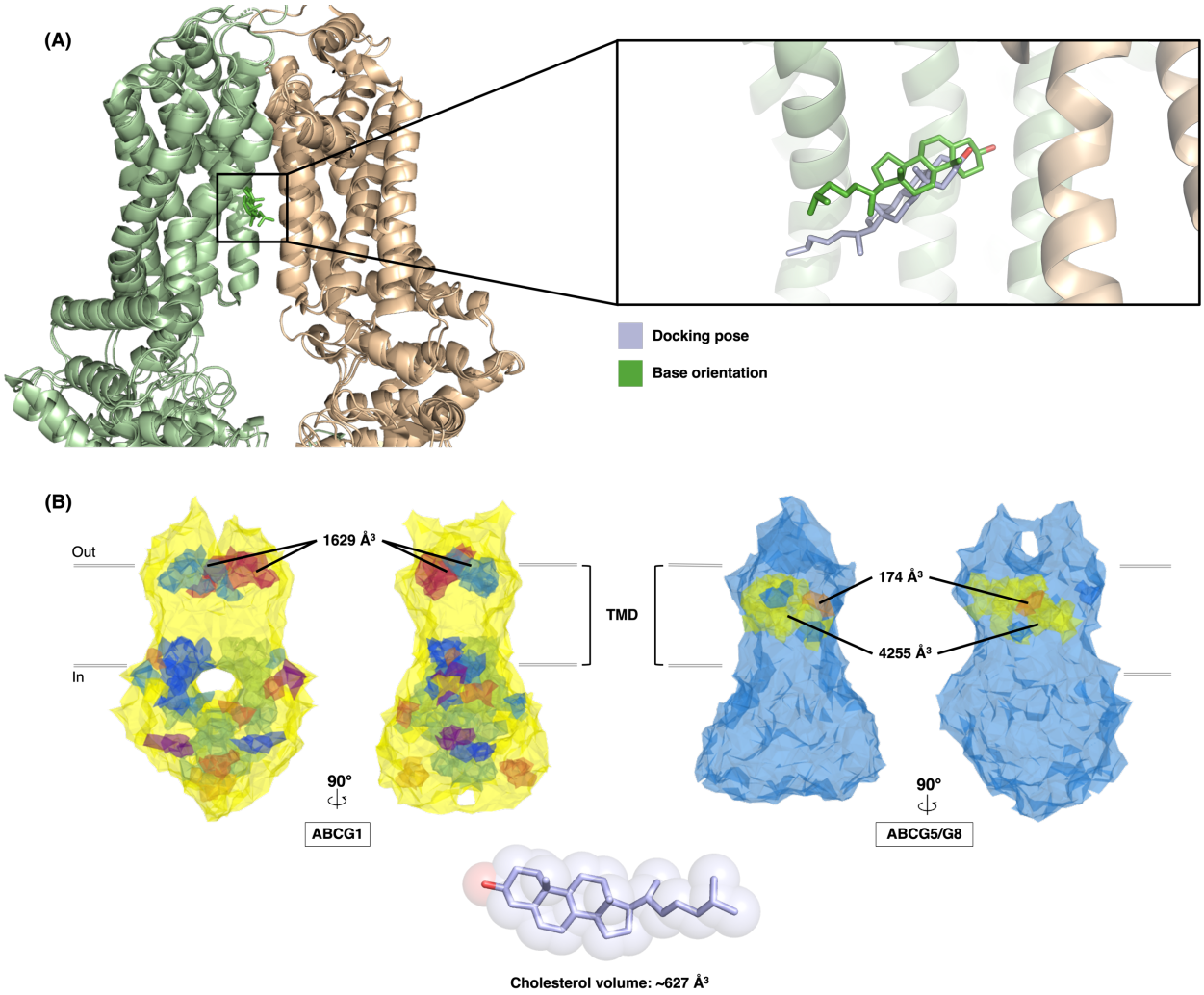

Supplemental Figure 5. Cavities and binding regions in ABCG structures. (A) *Left.* ABCG5/G8 (PDB ID: 5DO7) aligned with cryo-EM structure (PDB ID: 7R8D). *Right.* Comparison of cholesterol docking pose (light blue) with the cholesterol (green) in the cryo-EM structure [28]. **(B)** Volumes of transmembrane domain (TMD) cavities found in the of ATP-bound ABCG1 (yellow, PDB ID: 7R8E) and ABCG5/G8 (blue) calculated by MOLE2.5. *Left*, two cavities in ABCG1 found near the interface between the TMD and extracellular domain (ECD). These cavities (1629Å^3 each) curve over the central canal of the protein. *Right*, one large cavity found spanning throughout the TMD. This cavity represents a conglomeration of sphere-shaped cavities connected by thin bridging regions. Relevant cavities in the central canal of the protein are represented as spherical and estimated to be near the size of ~200Å^3. *Bottom*, the volume of a cholesterol molecule is 627Å^3.